Regional Dependence of Functional Connectivity in Cortical Microcircuits

by

John P. McCann

Bachelor of Philosophy, Neuroscience, University of Pittsburgh, 2024

Submitted to the Graduate Faculty of the

Dietrich School of Arts and Sciences in partial fulfillment

of the requirements for the degree of

Bachelor of Philosophy

University of Pittsburgh

2024

UNIVERSITY OF PITTSBURGH

DIETRICH SCHOOL OF ARTS AND SCIENCES

This thesis was presented

by

John P. McCann

It was defended on

April 9, 2024

and approved by

Chengcheng Huang, Assistant Professor, Department of Neuroscience

Bryan M. Hooks, Assistant Professor, Department Neurobiology

Christopher D. Harvey, Harvard Medical School, Professor, Department of Neurobiology

Thesis Advisor: Caroline Runyan, Associate Professor, Department of Neuroscience

Regional Dependence of Functional Connectivity in Cortical Microcircuits

John P. McCann, BPhil

University of Pittsburgh, 2024

The general structure of cortical microcircuits appears to be conserved throughout the cortical hierarchy; however, specific differences in functional properties of this stereotyped microcircuit across regions could contribute to the variety of computations performed by areas throughout the sensory processing hierarchy. This study investigated the functional connectivity of layer 2/3 excitatory neurons of primary auditory cortex (AC) and the posterior parietal cortex (PPC) through a combined approach of single cell optogenetic stimulation of excitatory neurons and 2-photon calcium imaging. Additionally, SOM inhibitory interneurons were specifically labeled in order to reveal potential differences between excitatory-excitatory and excitatory-SOM connections. To statistically characterize the influence of the photostimulation on the neural population, we utilized generalized linear models (GLMs). Our statistical approach revealed a strong inverse relationship between magnitude of influence and distance from the stimulated neuron; however, the influence had a broader spatial scale in PPC than in AC. Additionally, the spatial distribution of influenced neurons was significantly broader for SOM cells and negatively influenced non-SOM cells than positively influenced non-SOM cells in both regions. Interestingly, running modulation, calculated through GLMs, was concentrated in negatively influenced non-SOM cells in both regions suggesting a potential bias in inhibitory connections to running modulated neurons.

Table of Contents

List of Tables

List of Figures

List of Equations

Preface

I would like to acknowledge and thank Christine Khoury who performed the surgeries and collected the data analyzed in this study. I would also like to thank my colleagues at the Runyan lab for their insights and guidance. Specifically, I would like to acknowledge Dr. Runyan for her mentorship.

This research was supported in part by the University of Pittsburgh Center for Research Computing through the resources provided. Specifically, this work used the H2P cluster, which is supported by NSF award number OAC-2117681.

1.0 Introduction

1.1 Neural Basis of Perception

We are connected to the external world through our senses which transduce various forms of energy into electrical pulses encoding environmental information. A fundamental goal of neuroscience is to elucidate the methods that the brain employs to store, modify, and utilize sensory data. The complexity inherent in our environment requires the brain to coordinate actions with respect to multiple modalities of sensory information in addition to previous experience and internal brain state. Everyday tasks such as driving a car depend on the ability to quickly react to dynamic visual and auditory input as well as the ability to integrate that sensory data with prior experience and valence attributions. In order to efficiently accomplish such computationally complex tasks, the brain utilizes a hierarchical organization of structures which process subsets of information in a serialized manner (Banich & Compton, 2023). Recent work has questioned the rigidity of the canonical sensory hierarchy and emphasized the contributions of feedback projections from higher areas which meaningfully alter the activity of lower sensory regions (Herzog & Clarke, 2014; Walsh, McGovern, Clark, & O'Connell, 2020). An understanding of sensory processing at a systems level requires an understanding of regional and local network architecture. Regional connectivity provides a layout for the system, and local functional connectivity determines the computations performed by a region. Therefore, to precisely probe the theoretical descriptions of perception, a rigorous description of the local functional properties of cortical circuits is required.

1.2 Cortical Microcircuit

A canonical microcircuit circuit has been found across cortical regions despite the differences in functional roles of those regions (Harris & Mrsic-Flogel, 2013). Understanding the anatomical connections and the functional properties of this generalized cortical circuit is a critical step in describing how it performs computations on incoming sensory data. Additionally, insights into how these anatomical and functional properties vary across brain regions would help explain the wide range of emergent roles of a common circuit. The canonical cortical circuit is composed of both excitatory principal cells and various GABAergic inhibitory interneurons which follow a stereotyped connectivity pattern (Harris & Mrsic-Flogel, 2013). The connectivity patterns of excitatory pyramidal (PYR) neurons largely depend on the cortical layer in which their cell body resides. Layer four PYR cells receive feedforward input from thalamus or lower-level cortices, while layer 2/3 PYR cells receive local input from layer four PYR neurons and project to other cortical areas (Douglas & Martin, 2004). Layer five PYR neurons mainly project to subcortical structures and receive input from local cortical projections. PYR neurons are also generally recurrently connected in partially overlapping subnetworks restricted by distance (Yoshimura, Dantzker, & Callaway, 2005). The dynamics of cortical networks are complicated by GABAergic inhibitory neurons which add to the computational capabilities of the circuit.

Cortical inhibitory interneurons are numerous and highly diverse morphologically. With the use of genetic profiling, non-overlapping subsets of inhibitory interneurons have been described by the expression of the proteins somatostatin (SOM), parvalbumin (PV) and 5-HT3A-receptor expressing neurons which contains the subsets of vasoactive intestinal peptide (VIP) interneurons and neurogliaform cells (NG) (Harris & Mrsic-Flogel, 2013). These genetic divisions correspond to functional subtypes. Layer 2/3 PV neurons receive input from intralaminar and layer

4 PYR cells, and they characteristically make strong yet depressing synapses near the axon initial segment of PYR cells (Ma, Hu, & Agmon, 2012) which allows them to provide influential yet transient feedback inhibition onto PYR cells. SOM interneurons densely innervate nearby PYR neurons through synapses onto the distal dendrites (Fino & Yuste, 2011), and they pool their input from a wide range of neighboring PYR neurons by means of facilitating synapses (Yavorska & Wehr, 2016). Additionally, SOM neurons synapses onto PV interneurons providing an avenue for disinhibition of PYR neurons (Xu, Jeong, Tremblay, & Rudy, 2013). Additionally, SOM interneurons are linked together by gap junctions (Fanselow, Richardson, & Connors, 2008) which results in a coordinated inhibitory wave onto the PYR neural network. VIP interneurons are connected to the canonical circuit through facilitating inhibitory synapses onto SOM cells (Pfeffer, Xue, He, Huang, & Scanziani, 2013) which have been proposed to play a role in learning and attention (Natan et al., 2015). NG cells have a different function relative to the other inhibitory neurons in the circuit, for they have been found to release GABA by volume transmission and are proposed to modulate cortical activity through extrasynaptic effects (Oláh et al., 2009).

The described connectivity patterns have been proposed to shape the computations performed across cortical regions. In particular SOM interneurons have been demonstrated to contribute to lateral inhibition in V1 (Adesnik, Bruns, Taniguchi, Huang, & Scanziani, 2012) suppression of responses to repeated stimuli in primary auditory cortex (Natan et al., 2015), and recently a subtype of SOM interneurons has been found to contribute a specific error-correction signal in the posterior parietal cortex of mice (Green et al., 2023). Despite our current understanding of the canonical cortical circuit, further research is needed to describe how the functional response properties of different circuit components could contribute to the overall functioning of a brain region.

1.3 Auditory Cortex and Posterior Parietal Cortex

In this study we compare the effects of single cell optogenetic stimulation of PYR neurons in primary auditory cortex (AC) and posterior parietal cortex (PPC) on surrounding PYR and SOM neurons through 2-photon calcium imaging during passive behavior. The comparison between the regions provides an opportunity to investigate how the functional characteristics of cortical circuitry changes depending on the function of a region.

AC is a sensory cortex which receives auditory information relayed through the medial geniculate nucleus of the thalamus in addition to auditory information from the inferior colliculus (Stiebler, Neulist, Fichtel, & Ehret, 1997). Within AC, there exists a broad scale tonotopic map which represents the range of perceivable frequencies (Guo et al., 2012). The robustness of this tonotopic map at smaller spatial scales has been debated (Rothschild, Nelken, & Mizrahi, 2010), yet recent analysis has demonstrated that the degree of fine scale tonotopic mapping depends strongly on cell inclusion criteria. It appears that the mapping observed at a global scale persists at a finer spatial scale if analysis is restricted to highly tuned neurons, but the tonotopic map devolves as neurons with weaker sound responses are included in analysis (Romero et al., 2020). AC also performs computations on incoming sensory data such as attention-based gain control (Francis et al., 2018), suppression of repeated stimuli (Natan et al., 2015), and temporal modulation of stimuli through balanced excitation and inhibition (Wehr & Zador, 2003). The computational complexity implied by these findings emphasize the need for further investigation into the functional connections between neurons within AC to elucidate the circuit mechanisms underlying AC's representation of sensory stimuli and computations.

PPC serves a different purpose in the sensory hierarchy, for it receives processed sensory information of multiple modalities in addition to forming reciprocal connections with association

cortices (Hovde, Gianatti, Witter, & Whitlock, 2018). More specifically, PPC's sensory connections include reciprocal connections with the trunk and lower limb regions of primary and secondary somatosensory cortices (Zhang et al., 2016), primary visual cortex, primary auditory cortex, and to the lateral posterior nucleus of the thalamus (Hovde et al., 2018). While PPC forms reciprocal connections with sensory cortices, its function extends beyond pure sensory processing. In virtual reality decision making tasks PPC neurons have been demonstrated to respond in relation to the mouse's progression in the maze (Harvey, Coen, & Tank, 2012). The relationship of PPC activity to location is therefore distinct from the location related activity seen in hippocampal cortex place cells (O'Keefe & Dostrovsky, 1971), for it appears to encode for egocentric location. This depiction follows the findings in humans and primates which have implicated the parietal lobe as an important contributor to building several egocentric representations of the body in space (Colby & Goldberg, 1999). PPC's position in the sensory hierarchy insinuates its potential role as a transformer of sensory information into motor action based on decision making. PPC has been found to adjust the weights of stimuli in primary visual cortex in relation to artificially distorted perceptual experience (Yoshitake et al., 2013) which implies that PPC's role as a transformer of sensory information is dynamic. The extensive reciprocal connections PPC makes with sensory regions could result in learning dependent modulation of those regions. While it is disputed whether or not PPC itself is responsible for the computations resulting in a decision, it is apparent that inactivation of PPC results in inability to accurately perform sensory guided decision-making tasks, and that information representing navigational decisions can be decoded from PPC activity (Harvey et al., 2012).

The variation in function of PPC and AC provides an optimal comparison to probe the functional properties of cortical networks. In order to further describe the functional properties of

AC and PPC, we utilized single cell optogenetic stimulation to map the influence of single PYR neurons on the surrounding network. The technique of influence mapping is a recent advent in systems neuroscience mediated by optimized optogenetic proteins, modern imaging techniques, and cell type specific protein expression. Recent studies have performed influence mapping in primary visual cortex (Chettih & Harvey, 2019), and somatostatin cells in PPC (Green et al., 2023), yet it has not been performed for excitatory cells within PPC or AC. Similar to single cell influence mapping, *in vivo* ensemble cell stimulation has also been performed in V1 (Oldenburg et al., 2024). Outlining the influence of the activity of a single PYR neuron in a cortical network provides an optimal template for determining how a cortical region integrates incoming information because it limits the experimental manipulation to the activity of a single neuron. Isolating the effects of a single neuron allows us to interrogate the fundamental dynamics of the network. Understanding the way a single neuron contributes to the network will aid in our description of the organization of these networks and the computations that they are performing.

1.4 Experimental and Statistical Approach

In order to quantify the results of the optogenetic stimulation, we analyzed the results using trial-based influence metric which defines influence as the trial averaged change in activity from the pre-stimulation to the post stimulation period divided by the standard deviation of the change. In addition to this measurement, we utilized a generalized linear model (GLM) to quantify the statistical relationship between the optogenetic stimulation and neuronal activity. Using a GLM to quantify the response allows for the disentanglement of the running behavior of the mouse on the stimulation response, and it provides an opportunity to investigate the temporal properties of the

stimulation response. In addition to these immediate benefits, using a GLM to establish influence mapping allows for the opportunity to determine the relationship between stimulus response and additional factors such as coupling index, and task related variables.

In this study we probe the functional contribution of the activity of a single excitatory neuron to the activity of the surrounding neurons through single cell optogenetic stimulation and compare the observed effects between AC and PPC. As expected, influence is larger over distance in PPC than in AC. This larger spatial range of influence is consistent with the conception of PPC as a region where multimodal sensory information is integrated as compared to AC which is a primary sensory cortex. While influence in PPC extended over a larger spatial scale than AC the magnitude of influence decreases strongly with distance from the stimulated neuron in both regions. Despite this strong contribution of distance to the magnitude of influence, the spatial distribution of significantly influenced SOM neurons and negatively influenced non-SOM cells exhibited a relatively broad spatial range. The GLM approach allowed for the statistical quantification of running modulation which revealed that running modulation was highest in negatively influenced non-SOM cells. This concentration of running modulation in negatively influenced non-SOM cells, in combination with the tendency for running modulated targets to influence running modulated cells, suggests a potential connection between intralaminar inhibitory to excitatory connections and running modulated neurons. This potential functional network of intralaminar excitatory to inhibitory which suppresses running modulated non-SOM cells could contribute to the gain control of motor information in relation to other input information.

2.0 Methods

2.1 Animals and Surgical Procedures

All experiments and surgical procedures were reviewed and approved by the Institution Animal Care and Use Committee at the University of Pittsburgh. Mice utilized in this study were the F1 generation of a cross between homozygous SOM-cre mice (Sst-IRES-Cre, JAX Stock #013044) homozygous Ai14 mice (RCL-tdT-D, JAX Stock #007914) obtained from Jackson Laboratory, ME, USA. For the surgical procedure 4% isoflurane was used for the induction of anesthesia, and a constant rate of 1-2% was maintained for the duration of the procedure. The mice were mounted on a stereotaxic frame (David Kopf Instruments, CA), and ophthalmic ointment was used to cover their eyes (Henry Schein, NY). At the onset of the procedure, carprofen and dexamethasone (Covetrus, ME) were injected subcutaneously to modulate pain and inflammation. A 2 x 2mm craniotomy was made over both left AC (centered at 3.0 mm posterior and 4.3 mm lateral to bregma), and PPC (centered at 2 mm posterior and 1.75 mm lateral to bregma). A mixture of AAV1-synapsin-l-GCamp6f and pAAV-CamKIIa-C1V1(t/t)-mScarlet-KV2.1 diluted to a factor of ~$1x10^{12}$ vg/mL was pressure injected over 5 to 10 minutes for a total of about 60nl of virus. A micromanipulator (QUAD, Sutter, CA) was used to target the viral injections to about 250µm under the dura in both PPC and AC injection sites. The craniotomy was sealed using a drop of Kwik Sil (World precision Instruments, FL) covered by a glass coverslip (3mm) which was held in place by dental cement (Parkell, NY). Dental cement was also used to attach a one-sided titanium headplate to the right hemisphere of the skull. Mice were allowed to recover from

anesthesia before being returned to their home cage. Following the surgery, they received oral carprofen tablets for pain management for three days.

2.2 Two-photon Microscope

A resonant scanning two-photon microscope with a 16x water immersion lens (Nikon CF175, 16X/0.8 NA, NY) was utilized to image the mouse brain. The images were acquired at a rate of 30 Hz with a resolution of 512 x 512 pixels (corresponding to about 500 x 500μm). AC and PPC were imaged on different days at depths corresponding to layers 2/3 of the cortex (approximately 150 to 300μm deep). The angle of the objective was rotated to match the angle of the cranial window implant for region being imaged (35-45 degrees from vertical for AC and 5-15 degrees from vertical for PPC). GCamp6f expressed in all neurons under the synapsin promotor and transgenic TdTomato expressed in SOM cells was excited by a femtosecond infrared laser (Insight X3, Spectra-Physics, CA) tuned to 920nm to record excitation and cell type identity.

2.3 Imaging Protocol

Mice were imaged on a given day for about an hour during which a series of targets were repeatedly stimulated in a pseudorandom order (see section 2.4 for more detail). Imaging planes were selected based on the expression of viral GCaMP6f and mScarlet. Expression of mScarlet was differentiated from td-Tomato expression by collecting images with the excitation laser tuned to 800nm because td-Tomato is not effectively excited by 800nm. Each mouse and each window

were imaged multiple times, but the fields of view on each day differed slightly in plane depth and lateral/posterior locations. Fields of view were imaged until over-expression of GCaMP6f was observed indicated by a nuclear inclusion in multiple cells in the field of view. During each experiment, the activity of non-SOM and SOM neurons was imaged.

2.4 Stimulation Parameters

A separate laser path was used to stimulate the excitatory neurons expressing the red shifted opsin C1V1. A 1045 nm beam was controlled using a separate set of galvanometers than the imaging galvanometers in order to allow for independent movement of the stimulation pathway beam from the imaging pathway beam. The stimulation pathway was joined with the imaging scan path using a combining dichroic. Targets were chosen based on the presence of mScarlet expressed (assessed at 800nm) and qualitative analysis of GCamp6f expression and location in the field of view. The targets were stimulated in a pseudorandom order by a 13µm diameter spiral at 250 Hz for 100ms periods. Each target was stimulated an average of 116±31 times (averaged across AC and PPC datasets) during each imaging session. The specificity of the stimulation was assessed in separate control experiments in which the stimulation center point was progressively moved from the center of the targeted neuron. The responsiveness of the neuron to the stimulation was then related to the distance of the stimulation center point to the location of the neuron. The maximum distance between effective stimulation location and targeted cell location was about 2µm, but as a precaution cells within a 25µm radius of the stimulation were removed from analysis.

2.5 Data & Image Processing

Imaging datasets from 15 PPC fields of view and 11 AC fields of view were included from 9 mice. Datasets were excluded based on the quality of the field of view and the expression levels of GCaMP6f (fields of view with significant photobleaching were removed).

The raw calcium dynamic movies were collected and concatenated. The concatenated movie was then motion corrected, and underwent cell body identification, and fluorescence and neuropil extraction through the program Suite2p 0.9.3 in Python (Pachitariu et al., 2017). Suite2p performed the registration (accounting for motion in the field of view) and initial formation of regions of interest corresponding to predicted cell bodies in an unsupervised manner. The ROIs were then manually reviewed and selected using the Suite2p GUI to ensure only appropriate ROIs were classified as cells (dendritic processes were excluded). TdTomato cells were manually selected based on mean fluorescence in the red channel after bleed-through correction and ROI estimates performed by Suite2p. The returned timeseries of raw fluorescence for each ROI from Suite2p was corrected by subtracting 70% of the estimated neuropil fluorescence.

2.6 ΔF/F and Deconvolution

The neuropil corrected fluorescence was further processed by calculating the change in fluorescence divided by the baseline fluorescence of each cell (ΔF/F). ΔF/F for each cell was calculated for each frame with the baseline fluorescence being calculated as the eight percentile of that cell spanning 450 frames before and after the current frame. The ΔF/F timeseries was deconvolved to transform the fluorescence measurements into spike rate estimates using the

OASIS toolbox (Friedrich, Zhou, & Paninski, 2017). The results of the deconvolution algorithm were then filtered by a threshold of 0.05 to remove events of low magnitude. All calculations were performed on the binarized version of these results set at the threshold of 0.05 unless otherwise specified.

2.7 Trial-based Influence Calculation

Influence of a stimulation on the surrounding neurons was calculated based on the trialized stimulation response of each neuron. To calculate the influence of the stimulation of a particular target on a neuron, the trial averaged change in activity (mean activity 10 frames post stimulation subtracted from mean activity 10 frames pre stimulation) was divided by the standard deviation of the change in activity across trials. Significance of influence was then determined by a shuffle analysis.

Significance of trial-based influence was assessed by comparing the influence calculation of each neuron-target relationship with a distribution of influence values for each pair calculated based on data with the time points of the stimulation shuffled. Influence was recalculated for each neuron-target pair 1000 times with randomly shifted stimulus time points. The shuffling of the stimulation time points ensured that the recalculated influence would be taken at a random time point in the session not corresponding to that target's stimulation period. A cell was considered to be significantly positively influenced if its influence value was greater than zero and above the 97.5 percentile of the shuffled influence values. A cell was considered to be negatively influenced if its influence value was less and zero and less than the 2.5 percentile of the shuffled values.

2.8 Generalized Linear Model

2.8.1 Motivations for using a GLM.

The influence calculation described in section 2.7 determines influence by averaging changes in activity across all trials; however, it is possible that latent factors contribute to the trial-to-trial variability which the trial-based influence calculation averages out. One of these potential latent factors is the running behavior of the mouse. Given that both neurons in AC and PPC have been found to be modulated by running to different degrees (Khoury, Fala, & Runyan, 2023), there is a possibility that the influence metric especially for weakly influenced cells is significantly affected by running related activity of the neurons. As seen below in figure 1, a weakly influenced cell does not reliably respond to the target stimulation, and the running behavior across trials where its response varies is also variable. The GLM approach statistically confirms whether or not responses following the stimulation are truly caused by the stimulation, or if they could be explained by the mouse's running behavior.

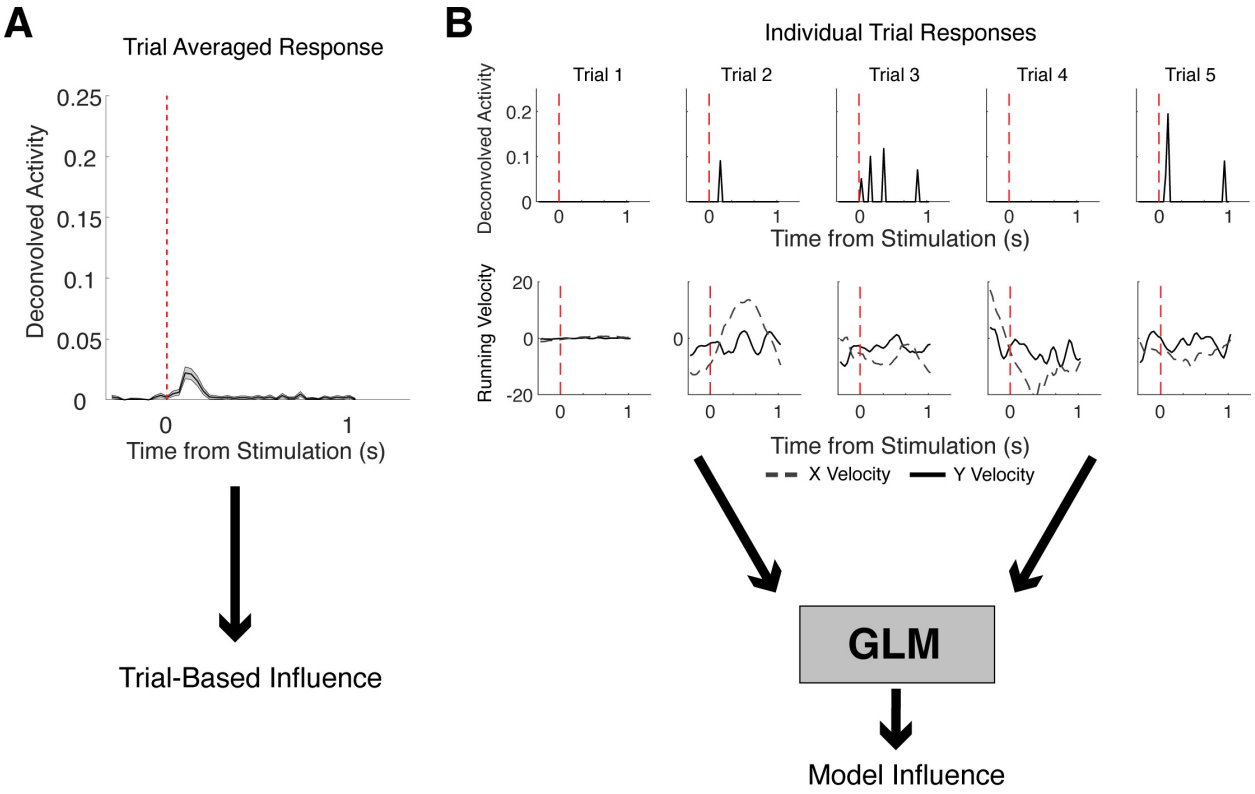

Figure 1 GLM accounts for trial-to-trial variability

(A) Trial averaged activity of an example PPC neuron is plotted. Dashed red line indicates time point of the stimulation. Grey shadding indicates SEM error. Response is averaged stimulation response from decovolved activity. (B) Top shows deconvolved activity for the same example PPC neuron shown on the left but for individual trials. Axis are the same as A. Bottom shows the X and Y running velocity of the mouse during each of the trials plotting directly above. X velocity is plotted with a dashed line, y velocity is plotted with a solid line.

2.8.2 Design Matrix

Two types of predictors comprised the design matrix: running related variables and stimulation related variables (Figure 2A). The mouse's running behavior was broken into forward,

backward, leftward, and rightward movement. These values were then normalized to have a range between zero and one. The activity in each of these directions was then convolved with eight gaussian temporal kernels. Four kernels extended in the retrograde direction spanning one second backwards in time from the current frame, and the other four kernels spanned one second forward in time (Figure 2B-C). The stimulation of each target was characterized by three gaussian temporal kernels with a maximum value of one spanning one second forward from the timepoint of the stimulation. Each of the stimulation related temporal kernels covers ten frames of the data (Figure 2D). Multiple temporal kernels were used for the stimulation predictors to investigate potential longer time scale effects of the stimulation, and to attempt to capture the shape of the stimulation responses.

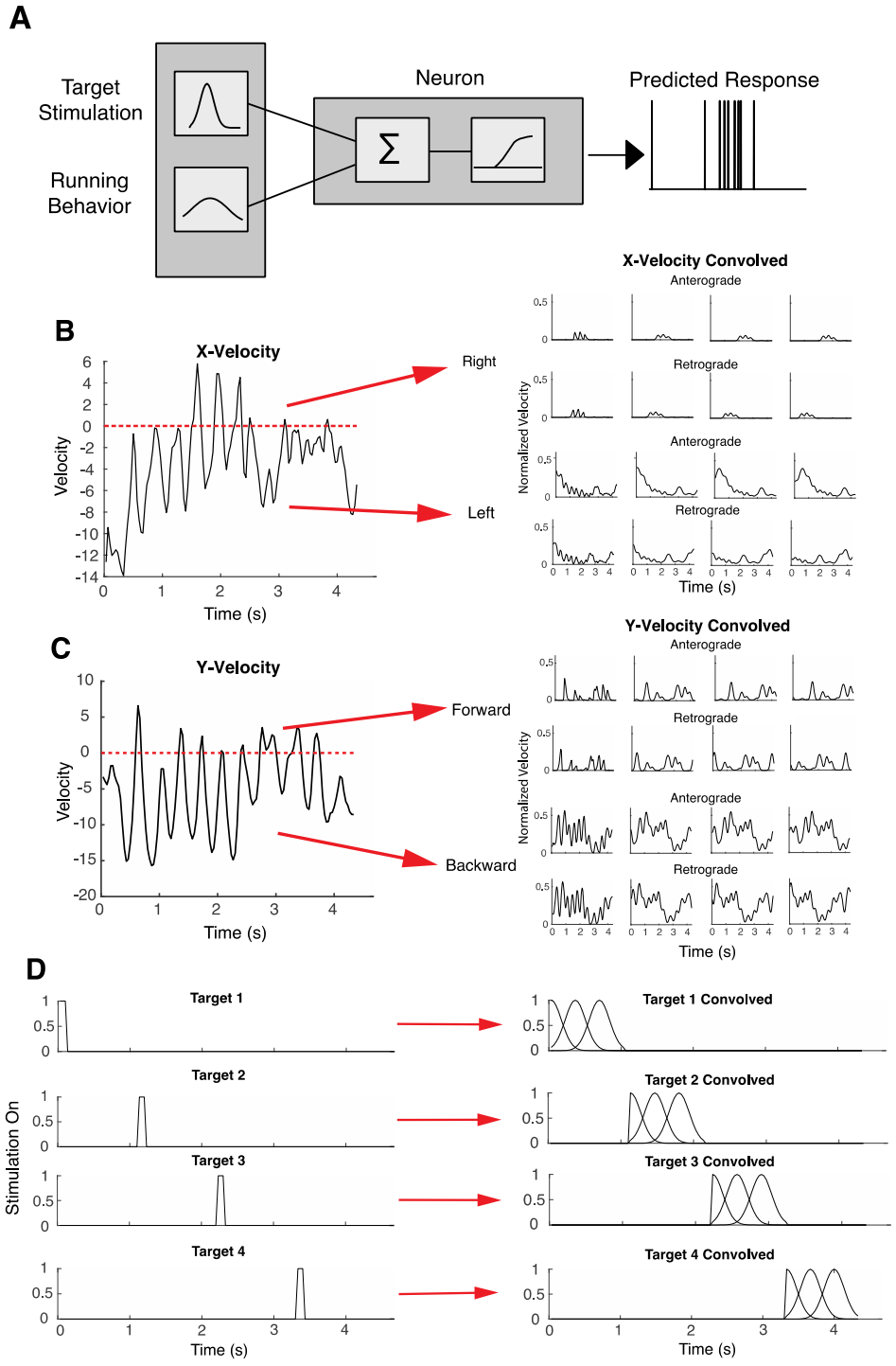

Figure 2 GLM structure and design matrix

(A) The GLM was fitted to each neurons activity with a combination of target predictors (modeling the stimulation) and running related predictors. (B) Left: example 4 seconds of X velocity of the mouse. Right:

top two rows are the convolved kernels of the positive X velocity or rightward motion. Bottom two rows are leftward motion. Each direction is convolved with 4 kernels moving forward in time from the current time point and 4 kernels moving backward in time from the current time point. Kernels are plotted from left to right in order of increasing time separation from current frame. All responses are normalized to be in the range of 0 to 1. (C) same as B but with Y velocity. (D) Left: Shows the time points when the stimulation is occuring (100ms). Same 4 seconds of the session as velocity plots are shown. Right: Shows the convolved predictors for each target. Each target has three predictors each spanning 10 frames in time aligned to the onset of the stimulus.

2.8.3 Glmnet and Regression

We isolated the contribution of the stimulation and running behavior on each neuron's activities using GLMs. We fit a binomial GLM to the binarized deconvolved activity of each neuron in the network using the package Glmnet (Friedman, Hastie, & Tibshirani, 2010). Glmnet fits the data via penalized maximum likelihood estimate. For our data we utilized the elastic net method with a regularization parameter of 0.25 which favors ridge regression. Ridge regression was favored because of the potential for multiple temporal kernels for the same target to contribute to explaining the activity of the cell. In almost all cases the first temporal kernel would have the highest weight due to the transient nature of the stimulation response, but the following temporal kernels contribute to the shape of the response and will likely be correlated with the first kernel. Therefore, we favored ridge regression which would bias against the model choosing a single temporal kernel for each neuron.

2.8.4 Cross Validation Methods

In order to prevent overfitting of the model, the data were split into train (70%) and test (30%) subsets for each dataset. The frames from each session were chunked into trials which were then segregated into the train or test subset. This separation of train and test trials was performed for ten folds for each dataset, and additionally, each fold of the train dataset was three-fold cross validated when the being fit.

2.8.5 Fitting Procedure

Glmnet utilizes a penalized maximum likelihood estimate to fit the data. The fitting was done on the University of Pittsburgh high throughput supercomputing cluster. Each neuron was fit and cross validated for a full model containing all of the running and stimulation predictors. Following the fitting of the full model, each neuron was then fit with a series of reduced models in which the predictors for a particular target were removed from the design matrix. A reduced model was fit for each stimulated target. Reduced models were also fit for the removal of all running related predictors and for the removal of all target related predictors.

2.8.6 Model Performance

The performance of the models was assessed through the fraction explained deviance measurement. The deviance of a given model was calculated as the difference in loglikelihood between the fitted model and the saturated model. Where $\ell(\hat{\beta})$ denotes loglikelihood as calculated

with the model fits, and ℓ_s denotes the loglikelihood of the saturated model which fits the data perfectly.

$$D = -2\left[\ell\left(\hat{\beta}\right) - \ell_s\right]$$ **Equation 1 Deviance**

To assess the performance of a given model, the measurement of fraction explained deviance was used. Fraction explained deviance was calculated as the deviance of the full model as a fraction of the deviance explained by the null model.

$$D_{Fraction} = \frac{D_{null} - D_{full\ model}}{D_{null}}$$ **Equation 2 Fraction Explained Deviance**

The model derived influence measurement was calculated as the change in fraction explained deviance between the full model and the reduced model. The model influence value for each neuron target relationship was calculated on test data not used in the model training process, and the resulting value was averaged across the ten cross validation folds. Additionally, only frames corresponding to time points of the stimulation trials for a given target were used to calculate the model influence for that target.

2.8.7 Simulated Cells

During the process of testing the GLM approach for characterizing influence, simulated cells were fit to investigate the specific contribution of mean session activity to the Δfraction explained deviance metric. Simulated cell responses were created to model a Poisson like distribution in response to the stimulation. The peak response was set to around four frames following the stimulation which mirrored the latency observed in real cells. A simulated cell was created by combining a set of three different simulated responses of different magnitudes. The ratio of this combination was varied across simulated cells to alter reliability and magnitude of

stimulation response. Random noise was then added outside of the stimulation response frames to achieve a predetermined mean session activity which was calculated outside of the stimulus response frames.

2.9 Histology

Each mouse used was transcardially perfused following the completion of all of their imaging sessions to ensure accurate viral targeting. Perfusions were performed with saline followed by 4% paraformaldehyde. Following the perfusion the brain was removed, and then cryoprotected, embedded, frozen and then sliced. The slices were mounted and stained with DAPI. Anatomical structures were used to verify the locations of viral injections in AC and PPC.

3.0 Results

3.1 Fields of View and Stimulation Controls

To investigate the difference in functional connectivity between AC and PPC, we used a combined approach of 2-photon calcium imaging and single cell optogenetic stimulation. Calcium dynamics were recorded through the indicator GCamp6f which was expressed in all neurons near the point of injection by means of the synapsin promotor. Cell type identity of SOM interneurons was determined by the expression of a red fluorescing indicator td-Tomato, which was transgenically expressed in SOM expressing interneurons. All neurons not expressing td-Tomato were considered excitatory neurons; however, a small number of these neurons were likely unlabeled inhibitory interneuron subtypes. Neurons were recorded from layer 2/3 (about 150-300 μm in depth) of AC and PPC while mice ran on a spherical treadmill (Figure 3A-B). The neural recordings were aligned to the stimulation timing and to the running behavior of the mouse. Data collected from nine mice were included in this study. Fields of view were 500 μm^2 for both regions, and in AC contained an average of 236 ± 117 neurons (±standard deviation) of which an average of 221 ±111 were non-SOM and 14±7 were classified as SOM interneurons. The PPC datasets contained an average of 259±88 neurons which on average was composed of 240±84 non-SOM neurons and 18±6 SOM interneurons. Analyses include 11 AC fields of view containing 2190 non-SOM neurons, 131 SOM neurons and 181 stimulation targets, and 15 PPC fields of view containing 3606 non-SOM neurons, 280 SOM neurons, and 278 stimulation targets. All analyzes were based on the deconvolved neural activity reported in arbitrary units. The deconvolved trace was binarized at a threshold (.05) in order to conform to the input

requirements of the binomial GLM. All analyzes which cite the trial-based influence calculation refer to the influence as calculated with the binarized deconvolved activity to reflect the data fitted by the GLM. Qualitative analysis of the ΔF/F traces revealed clear effects of the stimulation on surrounding neurons for both non-SOM and SOM cells (Figure 3C-D). The control experiments to determine the specificity of the stimulation revealed that removing neurons within 25µm from the target was a conservative correction for potential off target stimulation effects (Figure 3E).

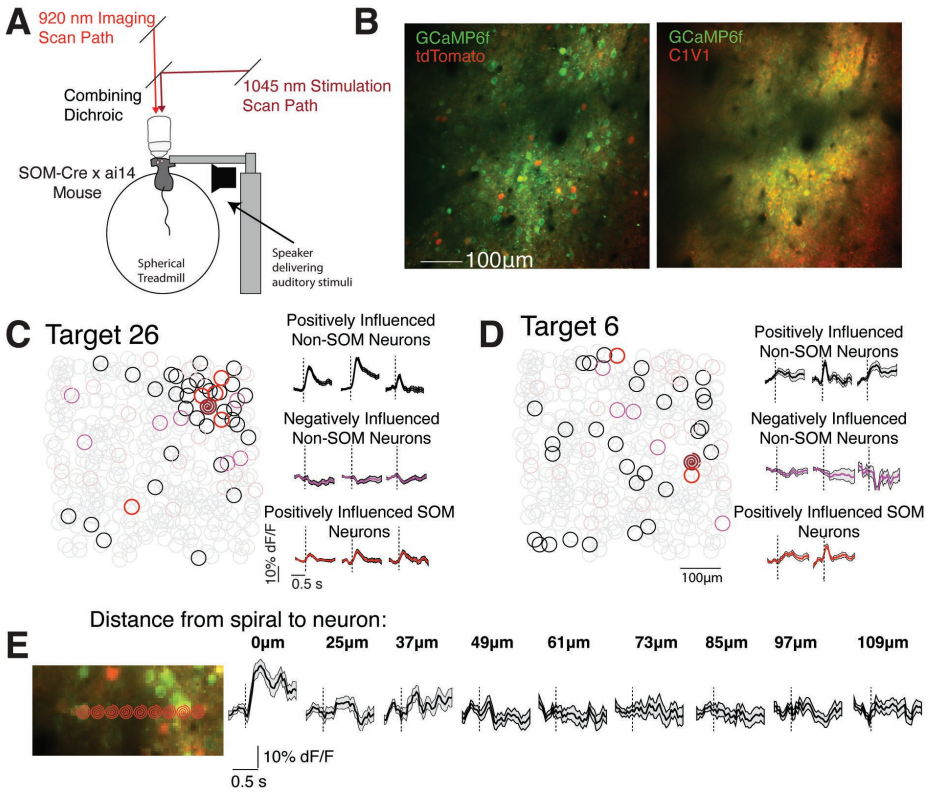

Figure 3 Experimental set up and stimulation controls

(A) An excitatory opsin (C1V1) was virally expressed in excitatory neurons. tdTomato was expressed transgenically in SOM neurons, and GCaMP was expressed in all neurons virally, in SOM-Cre x Ai14 mice. Mice ran voluntarily on a spherical treadmill throughout experiments. A speaker was used to present pure

tones to characterize auditory responses. (B) Left: Example field of view imaged at 920 nm, visualizing GCaMP (green) and tdTomato (red). Right: Same field of view, imaged at 780 nm, where the mScarlet (red, also expressed with C1V1) but not tdTomato can be visualized. (C) Left: Example influence map obtained from the field of view in B. Excited neuron's location indicated by the red 'spiral'. Significantly positively influenced neurons are circled in black, negatively influenced neurons in magenta. Right: Example trial averaged responses of significantly positively influenced E cells (black), negatively influenced E cells (purple), and positively influenced SOM cells (red) when this neuron was stimulated. (D) As in C, for another neuron that was targeted in the same session and field of view. (E) Control experiment to determine the spatial resolution of our stimulation. A neuron was stimulated and then spirals were targeted to adjacent locations, as indicated by the spirals. Right: Trial-averaged responses of the neuron under the left-most 'spiral'. The neuron was only significantly responsive when the spiral was focused directly on it. We only include other neurons that were at least 25µm away from the spiral in our influence measurements. According to our tests, this is a conservative enough approach because we rarely observe direct stimulation of a neuron even 2µm away.

3.2 GLM – Initial Fits of Reduced Models

In order to initially assess the validity of the GLM approach, the performance of a model with all target predictors and running predictors was compared against reduced models. To compare the performance of the two models we utilized the measurement of change in fraction explained deviance between the full model and the reduced model which contained a subset of the predictors in the full model (see equation 2). As seen in figure 5C-D, the full model strongly outperformed reduced models containing only running related predictors and only target related predictors in both AC and PPC. This indicates that those predictors meaningfully contributed to

the deviance explained by the model. The contribution of running predictors was compared to the contribution of target predictors in both regions in figure 5E revealing that running predictors contributed more to the deviance explained by the full model. The distribution of change in model performance with respect to the full model for the running subtracted model was right shifted as compared to the target subtracted model ($p < .0001$, Kolmogorov-Smirnov two sample test). The fraction explained deviance metrics for these comparisons were calculated using test data not utilized in the fitting process. Additionally, the model was able to effectively predict the time course of the neural response to the stimulus as seen in figure 4A-B.

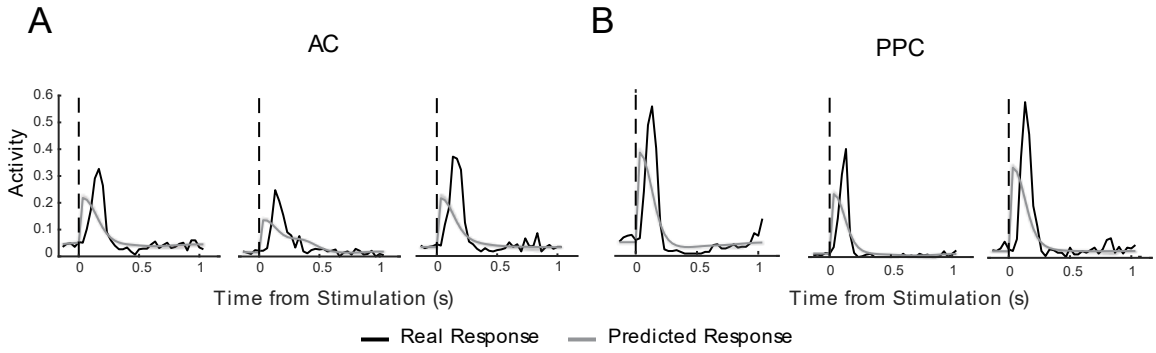

Figure 4 GLM predicts time course of stimulation response

(A) Predicted response traces in AC averaged over all trials in the test dataset. The predicted response is plotted in grey (calculated through the function cvglmnetPredict) and the observed deconvolved response is plotted in black. (B) Same as A but with PPC data.

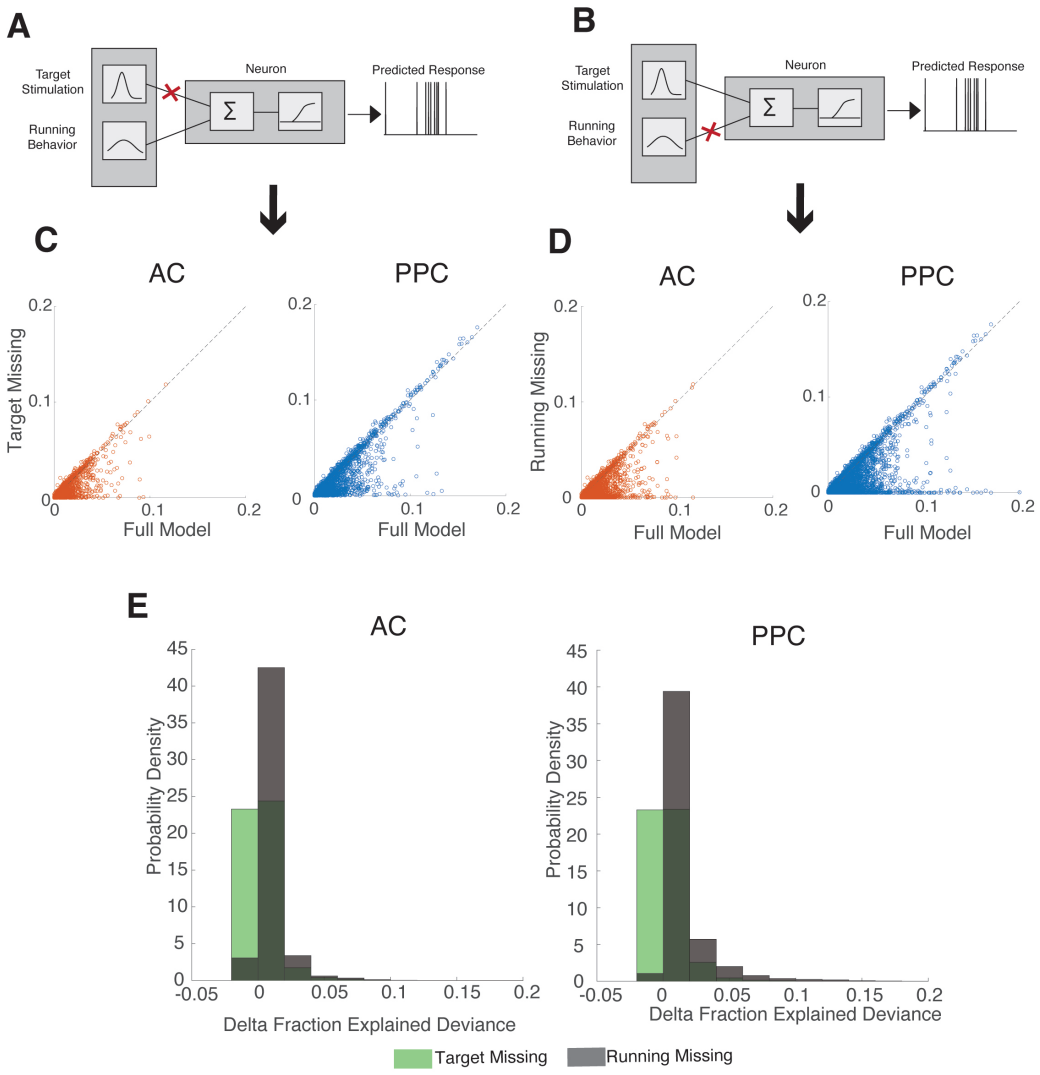

Figure 5 Running and target predictors contribute to deviance explained by GLM

(A) Graphical depiction of the target missing model whose fits are plotted in C. (B) Graphical depiction of Running missing model whose fits are plotted in D. (C) Performance of the full model plotted against the target missing model. Left: AC plotted in orange. Right: PPC plotted in blue. Select few well fit cells are cut off by axis limits. (D) Same as C but for the running missing model. (E) Probability density distributions of change in model performance as compared to the full model for the target missing and running missing models. The target missing model fits are plotted in green, and the running missing model fits are plotted in grey. Left: AC. Right: PPC.

3.3 GLM – Contribution of mean session activity to Model Influence

To calculate the specific contribution of the stimulation of a target to the model's ability to explain the activity of that neuron we fit a reduced model for each target. A metric of stimulation influence was derived through calculating the change in fraction explained deviance. Fraction explained deviance is dependent on the null deviance calculation (see section 2.8.6 Model Performance). Null deviance is calculated in same way as model deviance (see equation 1), but instead of utilizing the full set of parameters to calculate the loglikelihood, a single constant parameter is used. As seen below in figure 6, if the firing rate of a neuron is higher, then the null deviance will also be higher. This occurs conceptually because there is more variability in the neurons activity to explain when it fires more often; therefore, the null model is a worse fit for the data which causes a higher null deviance. Based on the calculation of fraction explained deviance (see Equation 2), a larger null deviance will necessarily result in a smaller fraction explained deviance for the same amount of deviance explained by the full model. This dependence could interfere with the ability to compare the magnitude of stimulation responses across cells because the same magnitude of response could be given a lower fraction explained deviance value if the neuron had a relatively higher mean session activity. Given the fact that the trial-based influence metric did not depend heavily on mean session activity (Figure 6B), we further investigated the dependence of the fraction explained deviance on mean session activity with simulated cell responses.

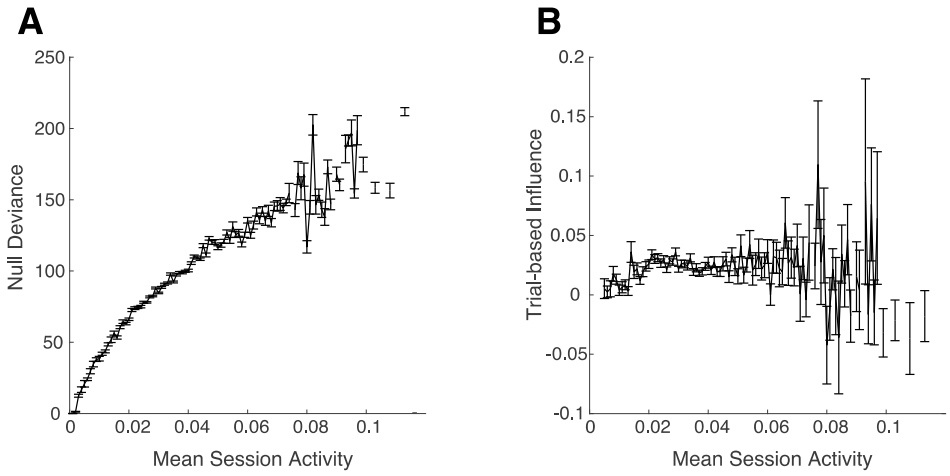

Figure 6 Null deviance increases with mean session activity

(A) Null deviance of the reduced models as a function of mean session activity. All fits from AC and PPC are included. Error bars are SEM. (B) Trial-based influence as a function of mean session activity (mean firing rate outside of frames in immediate stimulation response). All fits from AC and PPC are included.

Each simulated cell was fit three separate times with different levels of noise added to achieve three baseline firing rates. For a range of influence values, the model influence decreased with increases in firing rate (Figure 8B). The relationship between mean session activity and model influence was characterized by fitting a line to the distribution. The average slope of this relationship was -2.6. However, multiplying the model influence values by the square root of that neuron's mean session activity reduced the average slope to -0.06 (Figure 7C). All following analyses use the model influence multiplied by the square root of the non-stimulus-response firing rate of that neuron.

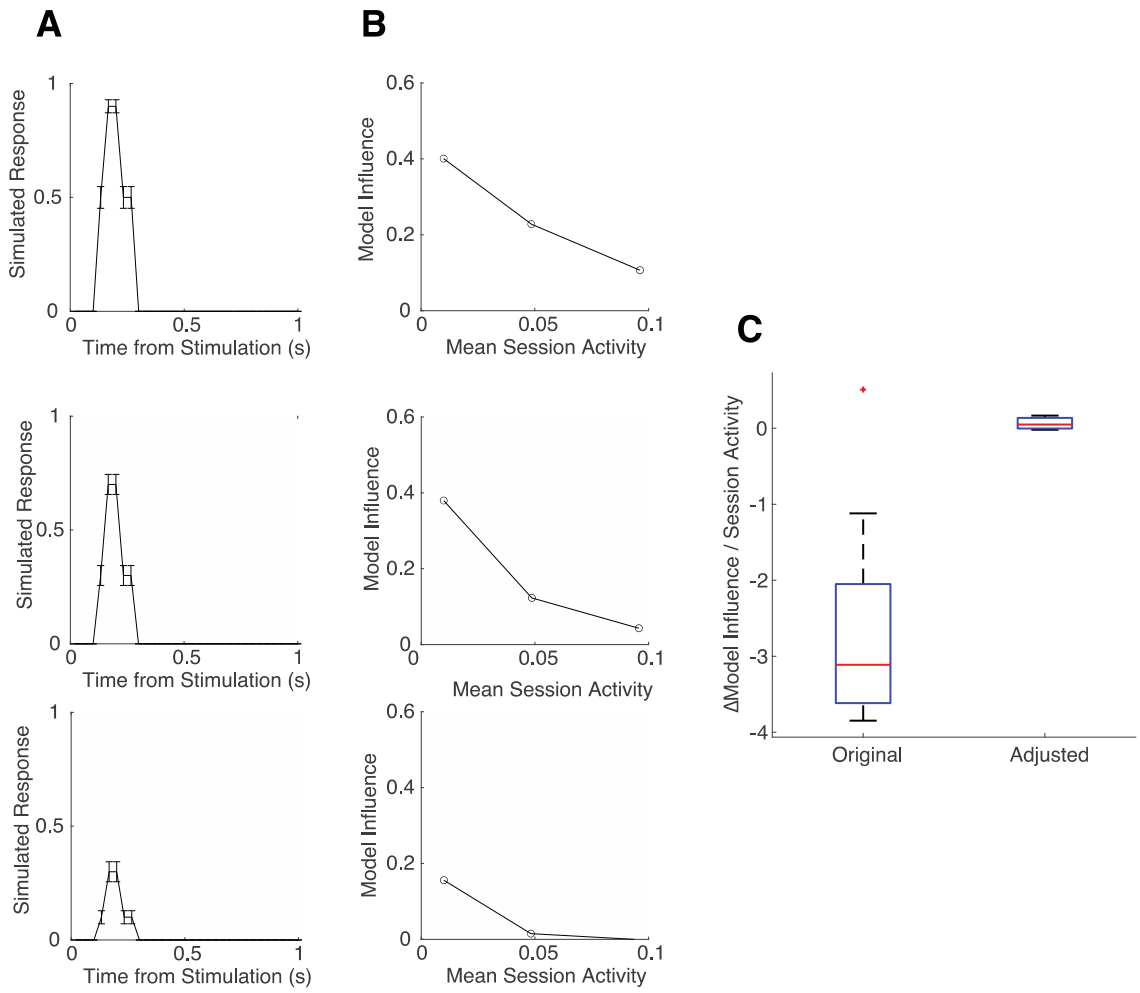

Figure 7 Simulations demonstrate model influence decreases with increases in mean session activity

(A) Trial averaged stimulus response of the simulated cells. Each plot is a separate simulated cell. Cell responses were simulated by combining different ratios of three response types. Responses were generated to follow a Poisson like distribution & generally match observed stimuli response timing. Error bars are SEM error. (B) Each simulated cell was fit to the full model and the reduced model with different levels of background firing, and the resulting model influence for each level was plotted against the background firing. The corresponding plot on the left is the stimulus response of the neuron being represented. (C) A line was fit to the points shown in panel B for a total of 15 simulated cells. The resulting slopes of those fits are plotted as a boxplot. The slopes were calculated again for model influence to background firing rate after the model influence was multiplied by the square root of the firing rate.

3.4 Comparison of Model Influence to Trial-based Influence

To further assess the GLM approach, the model influence measurement was compared to the trial-based influence metric (calculated as the mean change in activity from 10 frames pre stimulation to 10 frames post stimulation divided by the standard deviation of the change). A threshold of .005 in model improvement with target inclusion was applied to select for only substantially influenced cells. For cells above this threshold, the model influence was highly correlated to trial-based influence in AC ($r = 0.88$) and in PPC ($r = 0.90$) for positively influenced cells (Figure 8A). The correlation between model influence and trial-based influence was less strong for negatively influenced cells (Figure 8B) in both AC ($r = -.29$) and in PPC ($r = -.31$). When comparing the shuffle influence calculation for trial-based influence (see section 2.7) and the thresholded model influence, the model influence was generally more stringent. In the AC population (3163) marked significant by either metric, 34.2% of cells were marked as significant by both, 61.3% of the cells were included only by the traditional metric and 4.42% of cells were included only by the model threshold (Figure 9B left), and in PPC out of the combined 5313 neurons, 33.6% were marked as significant by both, 60.3% were included by only the traditional metric and 6.04% were included by only the model threshold (Figure 9B right). Additionally, the trial-averaged activity for each neuron in each of the three previously described groups of intersecting model and trial-based significance were plotted for both negative and positive influence (Figure 10). No substantial trends were noted between the two significance measures.

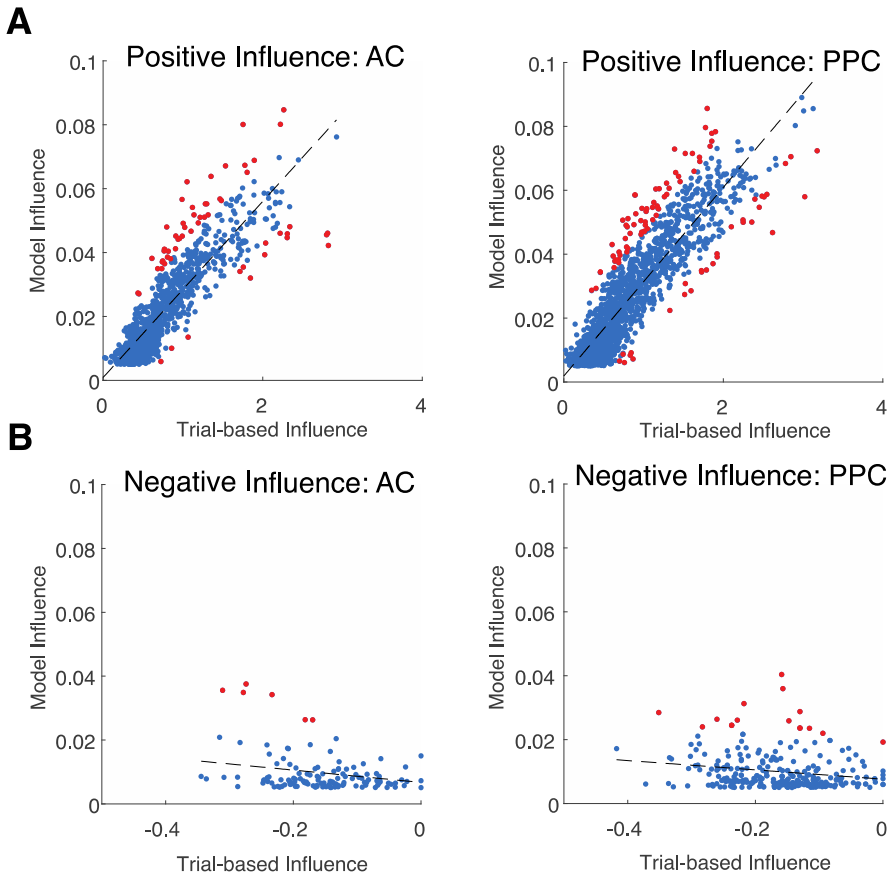

Figure 8 Model Influence is highly correlated to Trial-based Influence

(A) Model Influence plotted against trial-based influence for positively influenced cells above model influence threshold. Points were fit to a linear model. Fitted line plotted in black, and points plotted in red have residuals greater than two standard deviations. Left: AC. Right: PPC. (B) Same as A but with negatively influenced cells with model influence above threshold. Left: AC. Right: PPC.

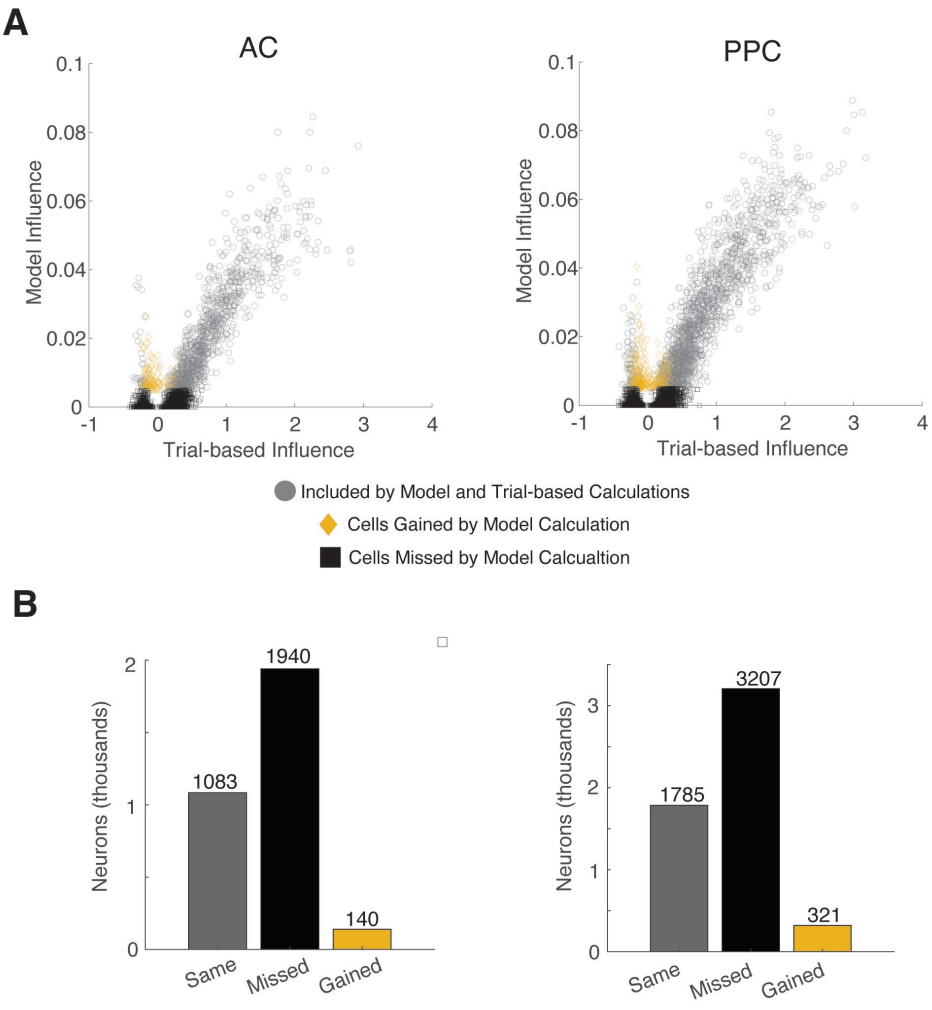

Figure 9 Model & Trial-based Influence Differ most for Weakly Influenced Cells

(A) Model influence is plotted against the trial-based influence value for each cell. Left: AC cells. Right: PPC cells. Points shown in grey demonstrated both significant influence and a model influence above threshold. Points in gold demonstrated a model influence above threshold, but not significant influence. Points in black demonstrated a significant influence value but not model influence above threshold. All influence values were calculated with binarized deconvolved data. (B) Bar plots of number of cells in each bin of overlapping significance shown in A. Colors correspond to the same groupings plotted in A. Left: AC. Right: PPC.

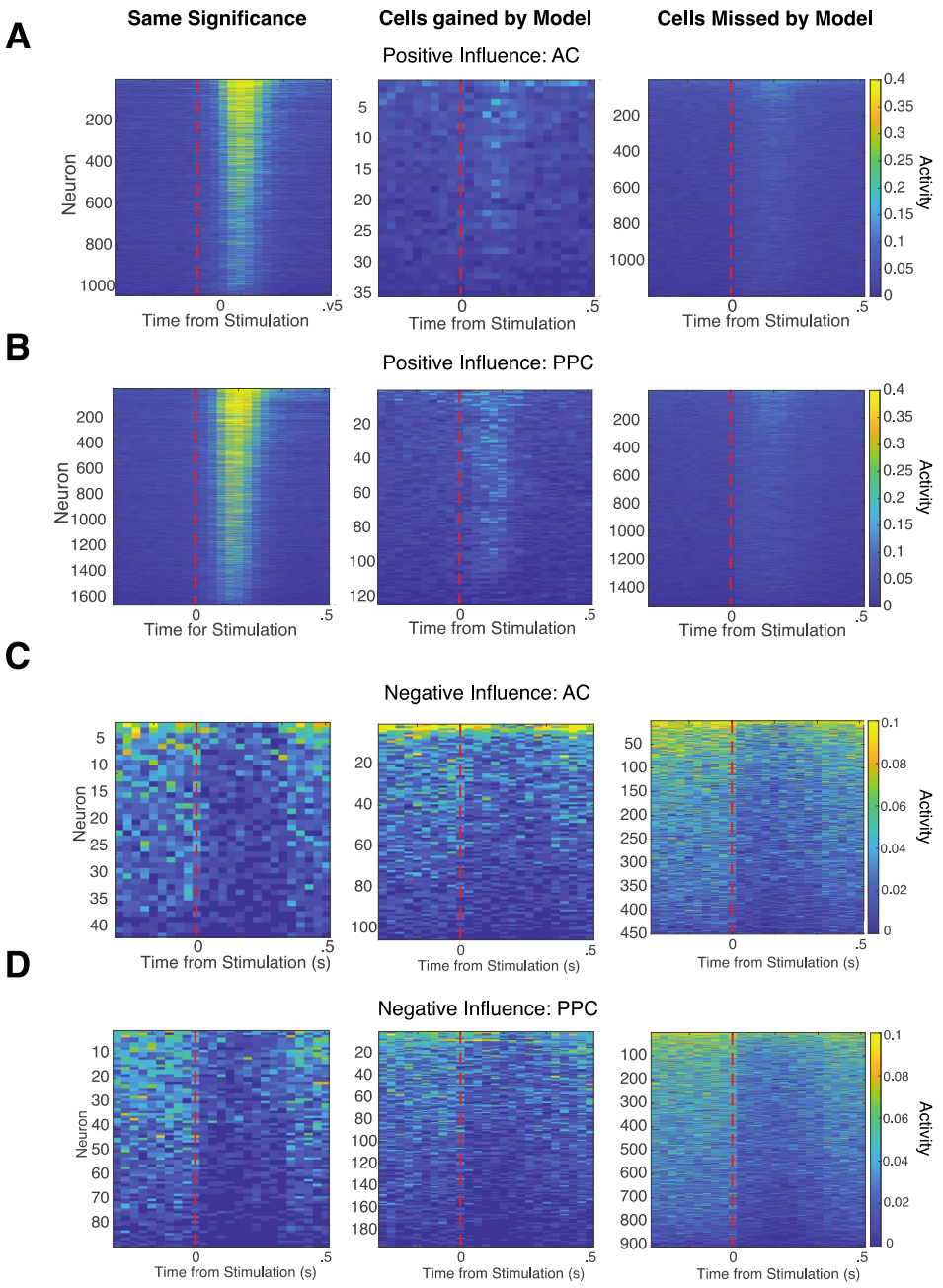

Figure 10 Trial Averaged Activity of Influenced Neurons

(A) Left: Trial averaged deconvolved activity of neurons in AC with significant influence and model influence above threshold. Red line indicates the time of stimulation. Middle: same as left but with neurons with model influence above threshold and not significant influence. Right: same as previous but with cells with significant influence and model influence below threshold. (B) Same as A but in PPC. (C) Same as A but with negatively influenced cells. (D) Same as C but in PPC.

3.5 Distribution of Model Influence with Respect to Distance from Stimulated Target

Given the different roles of AC and PPC in sensory processing, sensorimotor transformations and decision-making, the spatial span of influence could vary between regions to reflect the computations they perform. The variations in the spatial scale of influence in AC and PPC is further complicated by the subgroups of Non-SOM and SOM neurons and whether or not a cell is positively or negatively influenced by the stimulation of the target. As seen qualitatively in figure 11, the spatial range of negative influence is noticeably larger than positive influence, and the spatial range of positive influence on SOM interneurons appears to be larger than that of non-SOM neurons. When considering the difference in magnitude of all influence over distance between AC and PPC (Figure 12A), PPC had a significantly larger initial magnitude for non-SOM cells between 25 and 45 microns from the target ($p<.05$, post hoc multiple comparison test) and maintained this difference for the next distance bin of 45 to 65 microns ($p<.001$, post hoc multiple comparison test). This significant difference was not observed specifically for SOM cells between the two regions, but the overall contribution of the interaction between brain region and distance from stimulation target on influence was significant ($p=.0063$, 3-way anova) with PPC expressing a higher magnitude of influence over distance than AC. Additionally, within the first distance bin (25 through 45 microns), non-SOM cells in PPC expressed a significantly larger magnitude of influence than SOM interneurons in PPC ($p<.01$, post hoc multiple comparison test, Figure 12C), but this difference in influence magnitude across cell types was not maintained over distance.

Within AC there was not a significant difference between the magnitude of influence between cell types (Figure 12B).

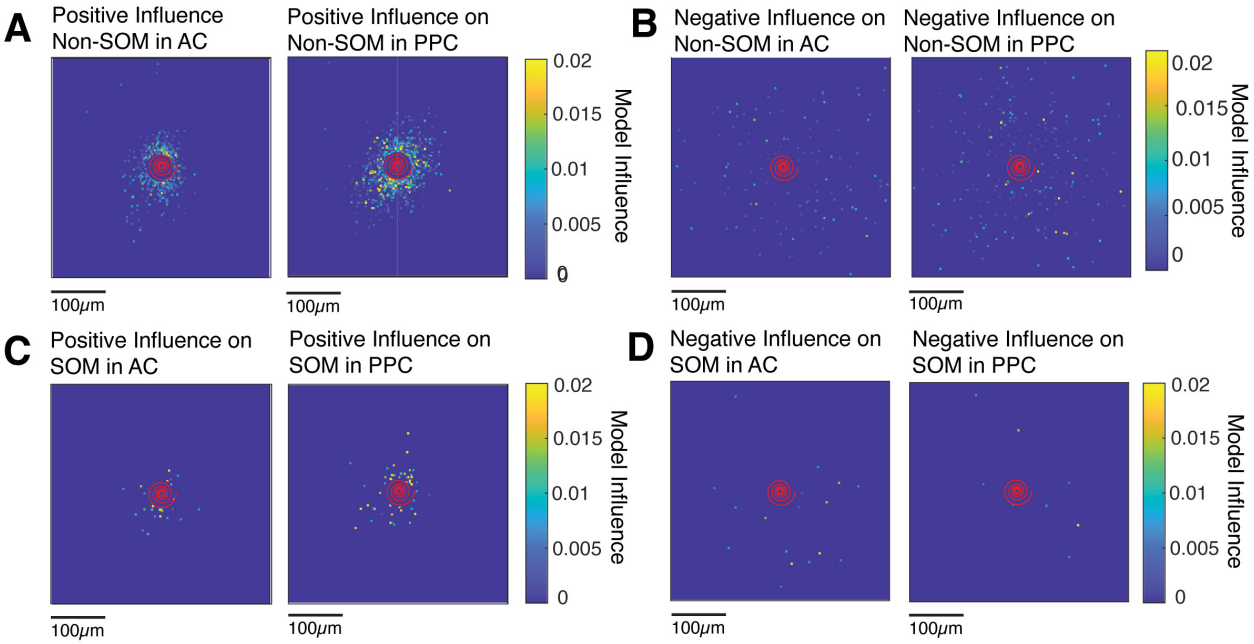

Figure 11 Spatial distribution of influence differs by cell type and influence sign

(A) Spatial distribution of positive influence on non-SOM neurons. Target location was centered, and coordinates of cells were adjusted to be relative to the center of the plot. Each cell was assigned a 2x2 pixel box centered on its x,y coordinates, and average influence value at each location on the grid was calculated. Left: AC. Right: PPC. (B) Same as A but with negatively influenced non-SOM neuron locations set to 1. (C) Same as A but with positively influenced SOM neuron locations set to 1. (D) Same as A but with negatively influenced SOM neuron locations set to 1.

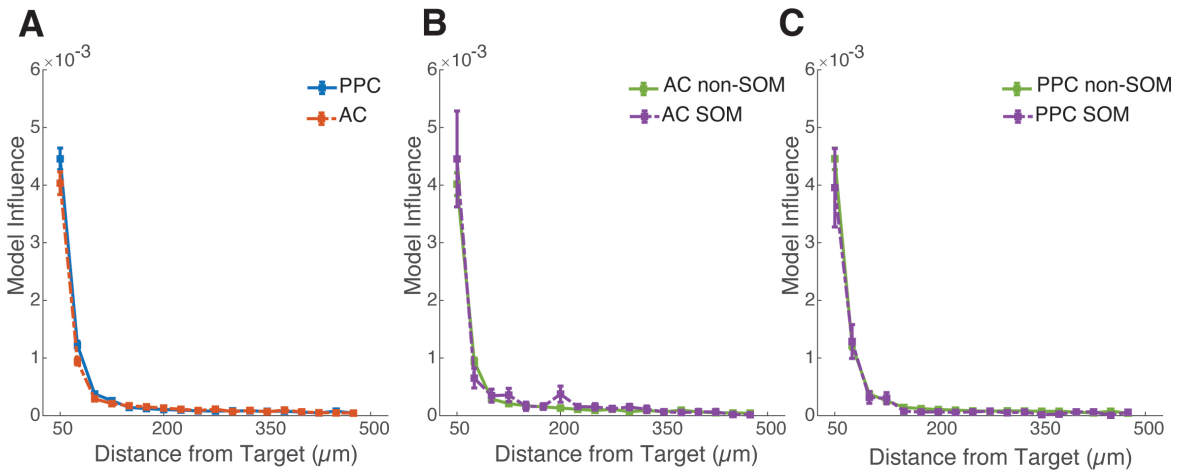

Figure 12 Magnitude of influence decreases with distance

(A) Average magnitude of influence over distance in AC vs PPC. Neurons within 25µm of the target were excluded from analysis. Each point is the average model influence of all cells in bins of 20µm spanning from 25µm to 500µm from the target. Error bars are SEM. AC is plotted in orange and PPC is plotted in blue. (B) Same as A but comparing the magnitude of influence of AC non-SOM and AC SOM cells as a function of distance. Non-SOM is plotted in green, and SOM is plotted in purple. (C) Same as B but comparing PPC non-SOM and SOM neurons. See appendix A for detailed statistics results.

A clear difference presented in the spatial distribution of model influence between positively influenced non-SOM cells, negatively influenced non-SOM cells, and positively influenced SOM cells. Figure 13 shows the probability density of cells with model influence above threshold with respect to distance for each of those subgroups with 95% bootstrapping confidence intervals. In both AC and PPC negative influence is more broadly distributed spatially than positive influence, and positive SOM cell influence follows this pattern of spatially extended influence (negative SOM influence excluded due to low n).

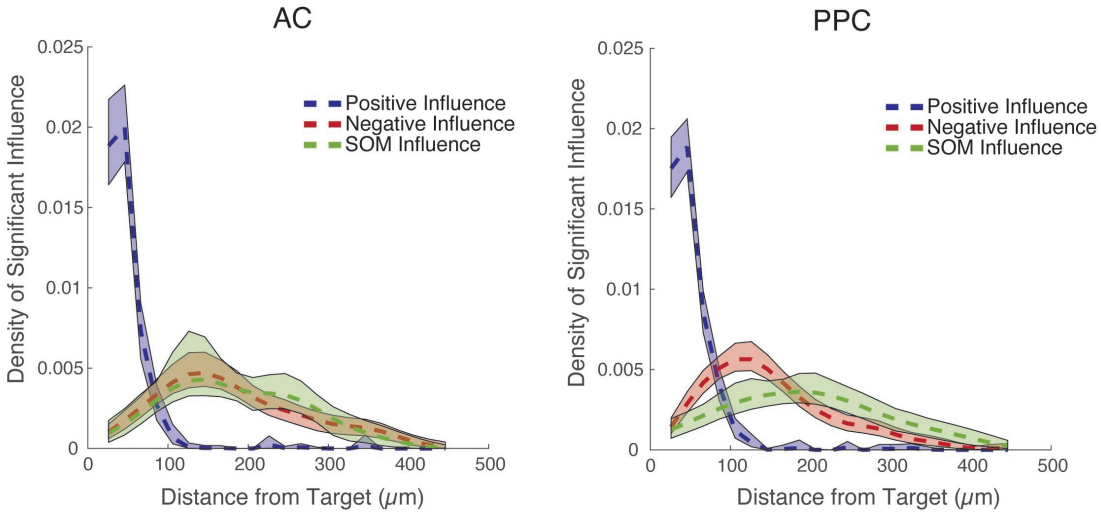

Figure 13 Distribution of Influence is broader for negatively influenced non-SOM and SOM cells

Distribution of significantly influenced cells (model influence above threshold) as a function of distance for positively influenced non-SOM, negatively influenced non-SOM and SOM cells. Probability density was calculated as a kernel distribution with kernels calculated at intervals of 20µm ranging from 25µm from the target to 480µm from the target. 95% bootstrapping confidence intervals are plotted as the shaded regions surrounding the curves. Distribution of positive non-SOM influence is plotted in blue, negatively non-SOM influence in red, and positive SOM influence in green. Left: AC. Right: PPC.

3.6 Interaction between Running Modulation and Model Influence

A strength of the GLM approach is the ability to characterize a neurons modulation by running in addition to target influence. A neurons running modulation was calculated as the change in fraction explained deviance between the full model and a model lacking all running predictors. As seen in figure 5B, the running subtracted models performed worse than the full model on most cells which indicates the presence of significant running related activity in both AC and PPC.

Running modulation was present in PPC at a higher level than AC (Figure 14). In AC, 3% of neurons were strongly modulated by running (considered as greater than 2% improvement in model performance with inclusion of running predictors) and an additional 4% were modulated by running and influenced by at least one target. In PPC, 8% of neurons were strongly modulated by running alone and an additional 5% were modulated by running and influenced by at least one target. In both regions more neurons were only influenced by at least a single target and not by running (22% AC and 19% PPC). Qualitatively (Figure 15), running modulation appears to be highest in negatively influenced cells, and overall, there is not a significant trend in the relationship of influence magnitude to running modulation magnitude. Also, positively influenced SOM cells did not appear to have a qualitatively different distribution of running modulation as positively influenced non-SOM cells (Figure 15). To further investigate the relationship of running modulation and influence, the cumulative distribution of running modulation was plotted for positively, negatively, and non-influenced cells (Figure 16). Negatively influenced cells had a distribution of running modulation with an average significantly higher than both non-influenced and positively influence in both AC and PPC. Statistical analysis revealed that the combination of cell type and sign of influence was significant in relationship to running modulation (AC: p = near 0, PPC: $p = 0.081$; 3-way anova). Specifically, negatively influenced non-SOM cells demonstrated the largest mean running modulation in AC and PPC. The difference in running modulation between negatively influenced SOM cells and positively influenced/non-influenced SOM cells was not significant in either region (see appendix B for full values).

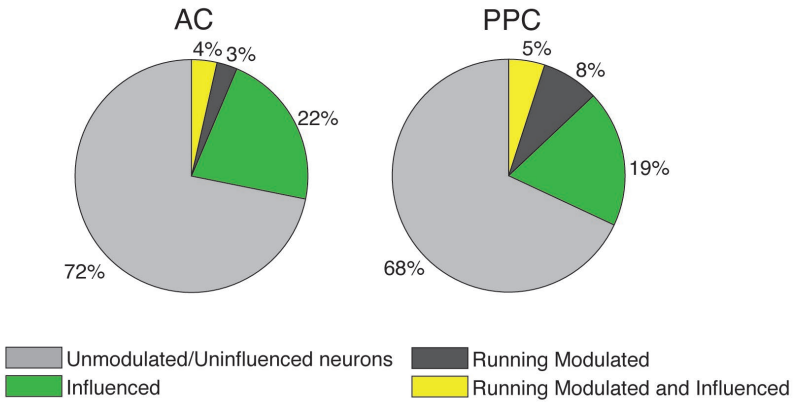

Figure 14 Running Modulation is greater in PPC than in AC

Percent of all cells either significantly influenced by at least one target and not modulated by running, cells modulated by running and not influence, cells modulated by running and influenced, and cells not significantly affected by either. Left: AC. Right: PPC. Running modulated determined by thresholding the Δfraction explained deviance when comparing the full model to the model lacking all running predictors.

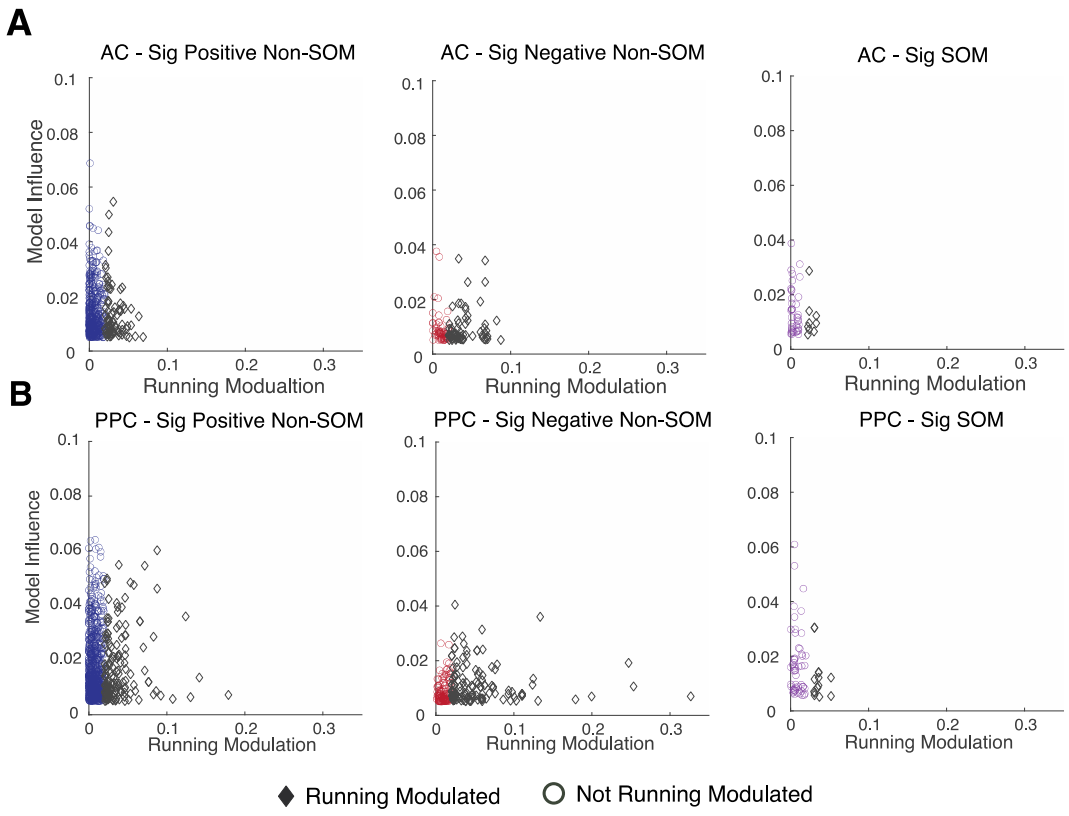

Figure 15 Relative running modulation by cell type & influence sign is similar across regions

(A) Value of model influence plotted versus value of running modulation for influenced neurons. Points plotted in black are above the threshold for significant running modulation. Left: positively influenced non-SOM cells in AC. Middle: negatively influenced non-SOM cells in AC. Right: influenced SOM cells in AC. (B) Same as A but in PPC. See appendix B for detailed statistics results.

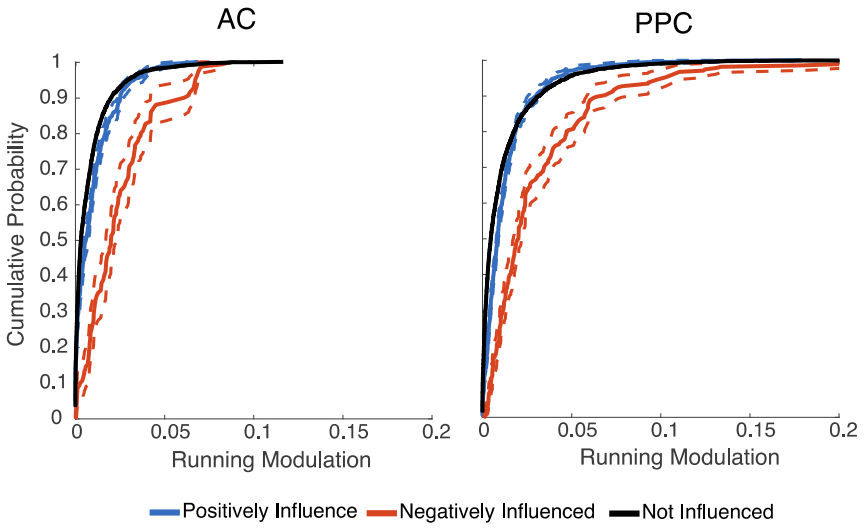

Figure 16 Running Modulation is greatest in Negatively Influenced Cells

Cumulative distribution of running modulation for positively influenced cells (blue), negatively influenced cells (red) and un-influenced cells (black). Dashed lines indicate 95% confidence intervals. Left: AC. Right: PPC.

Cells with similar tuning and theoretically input have been proposed to have a higher probability of recurrent connections (Ko et al., 2011; Lee et al., 2016). Due to this proposed framework, we then tested to see if cells that were influenced and modulated by running tended to be influenced by targets that were themselves modulated by running. Shared running modulation could suggest shared input sources, and therefore, could increase the probability of a connection between those neurons. As demonstrated by figure 17, in AC the ratio of cells modulated by running to unmodulated was significantly greater ($p = 0.003$, Wilcoxson rank sum) for cells influenced by targets also modulated by running (31.98 ± 4.43% SEM error) as compared to cells that were not modulated (18.68 ± 2.21%). In PPC the average ratio of modulated to unmodulated cells for running modulated targets (34.64 ± 5.02%) was greater than that of unmodulated targets

(26.01 ± 2.21%), yet this difference was not statistically significant (p = 0.1035, Wilcoxson rank sum).

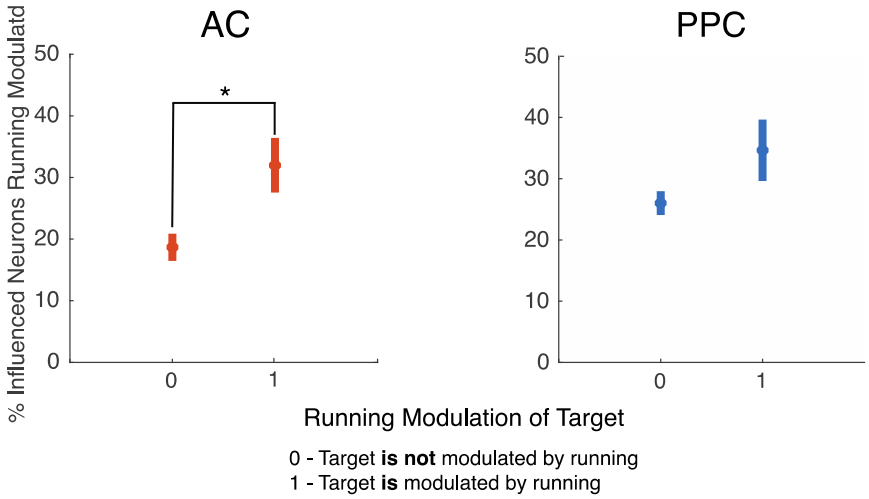

Figure 17 Running Modulated Targets tend to Influence Running Modulated Cells

Percentage of influenced cells with running modulation for targets with and without running modulation. Error bars are SEM. * denotes p<.05 for Wilcoxson rank sum test. Left: AC. Right: PPC.

Given the tendency observed in AC for neurons with running modulation to be influenced by targets that also demonstrate running related activity, we then investigated for either a cell type or influence sign trend within this relationship. Four subsets were defined as all the potential combinations running modulation of influenced neuron and its target. The relative percentage of non-SOM cells to SOM cells did not depend strongly on the relationship of target running modulation to influenced neuron running modulation (Figure 18). However, in line with figure 16, negatively influenced cells were overrepresented in neurons that were strongly modulated by

running (Figure 19). Negatively influenced neurons were overrepresented regardless of the running modulation of the target in AC and PPC.

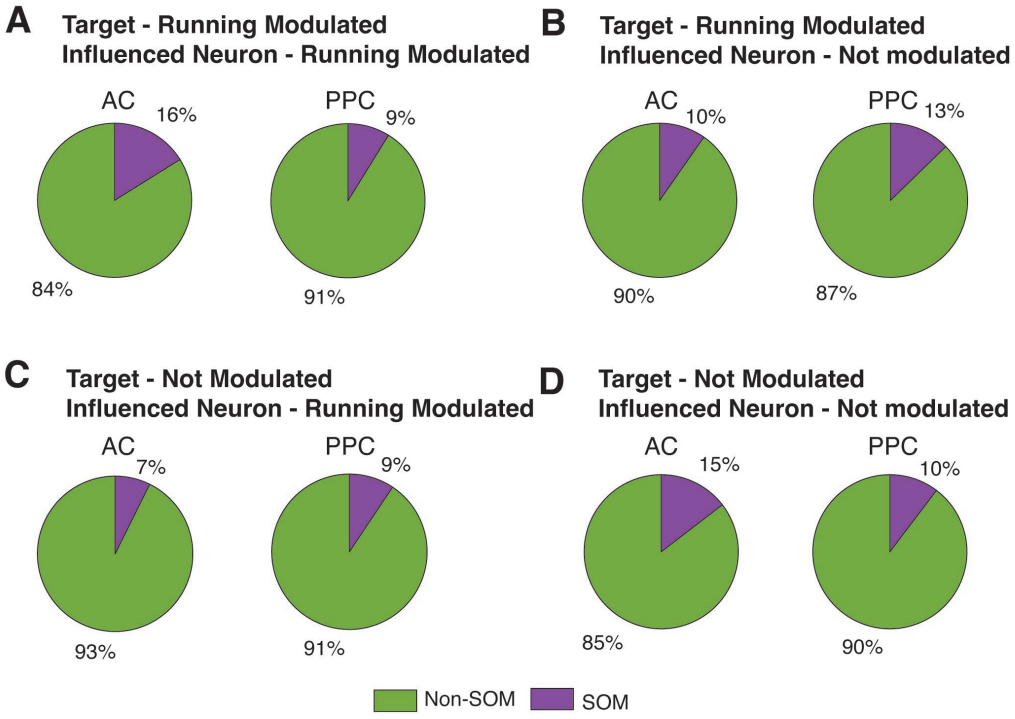

Figure 18 Relationship of running modulation of target to influenced neuron is not cell type specific

(A) Percentage of non-SOM cells to SOM cells for subset of neurons with running modulation that were influenced by a running modulated target. (B) Same as A but for cells not modulated by running but influenced by a running modulated target. (C) Same as A but for cells modulated by running and influenced by a target not modulated by running. (D) Same as A but for cells not modulated by running influenced by targets not modulated by running.

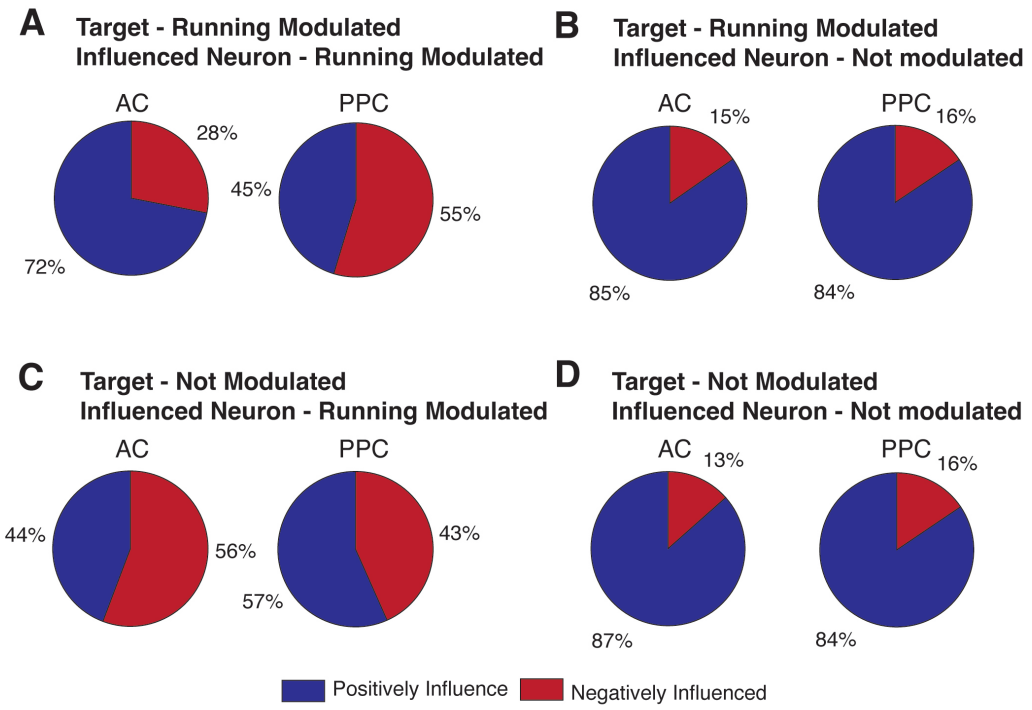

Figure 19 Running modulation is biased towards negatively influenced cells regardless of running modulation of target neuron

(A) Percentage of positively influenced cells to negatively influenced cells for subset of neurons with running modulation that were influenced by a running modulated target. (B) Same as A but for cells not modulated by running but influenced by a running modulated target. (C) Same as A but for cells modulated by running and influenced by a target not modulated by running. (D) Same as A but for cells not modulated by running influenced by targets not modulated by running.

Another potential indication of the significance of the relationship of running modulation between target and influenced neuron would be an increased magnitude of influence for neurons that shared the running modulation of the target. In both AC and PPC the magnitude of influence for positively/negatively influenced non-SOM cells and positively influenced SOM cells did not depend significantly on the relationship of running modulation between the influenced neuron and target (Figure 20). The only significant dependence of running modulation on influence magnitude

was a running modulation dependent increase in average influence for negatively influenced non-SOM cells with un-modulated targets ($p = 0.0011$ Wilcoxson rank sum test).

Influence is strongly dependent on distance from the targeted neuron in both AC and PPC; therefore, a change in the relationship of influence and distance based on the running modulation of the targeted cell would reveal an interaction between these two variables. Given the already wider distribution of negative influence as compared to positive influence, we restricted the analysis to positively influenced non-SOM neurons. In AC the distribution of significantly influenced cells for targets with running modulation was not significantly different from the distribution for targets without running modulation (Figure 21; $p = 0.2612$, Kolmogorov-Smirnov test). However, in PPC, running modulated targets demonstrated a distribution of influenced cells that was significantly broader spatially than that of targets not modulated by running (Figure 21; $p = 0.00036$, Kolmogorov-Smirnov test).

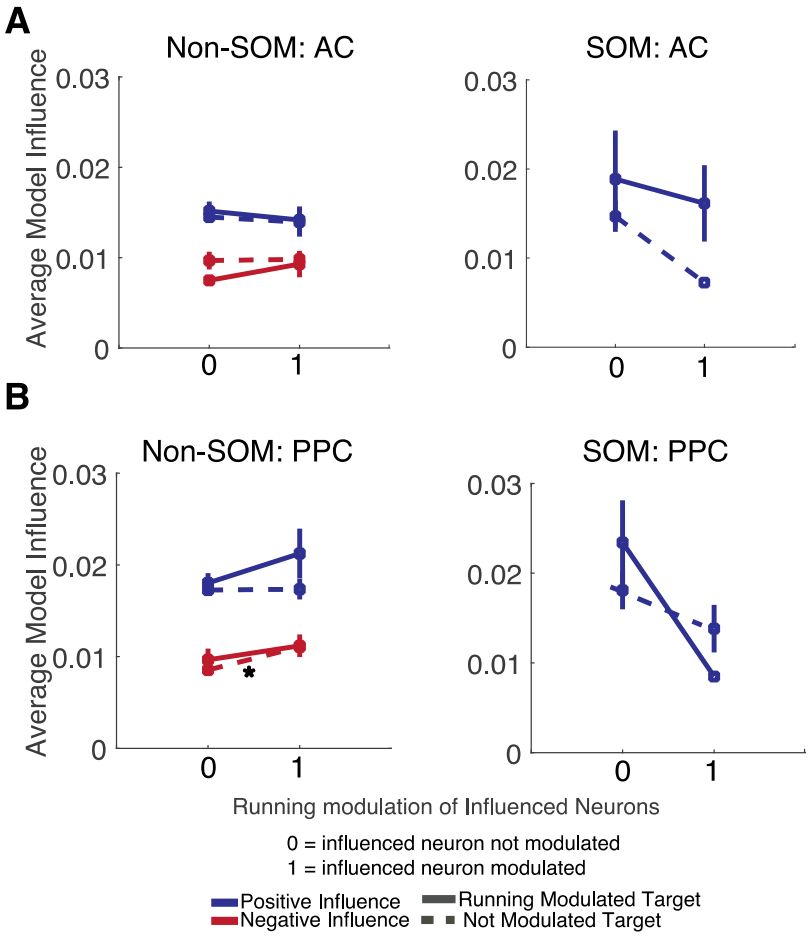

Figure 20 Magnitude of Influence does not depend on relationship of running modulation between target and influenced neuron

(A) Average influence of subsets of non-SOM cells in AC. Subsets defined by relationship of running modulation of the target and the running modulation of the influenced neuron. Running modulation of influenced neurons is denoted on X axis, running modulation of target is denoted by line style (solid line means running modulated target, dashed line means un-modulated target). Blue denotes positively influenced cells, red denotes negatively influenced cells. (B) Same as A but in PPC.

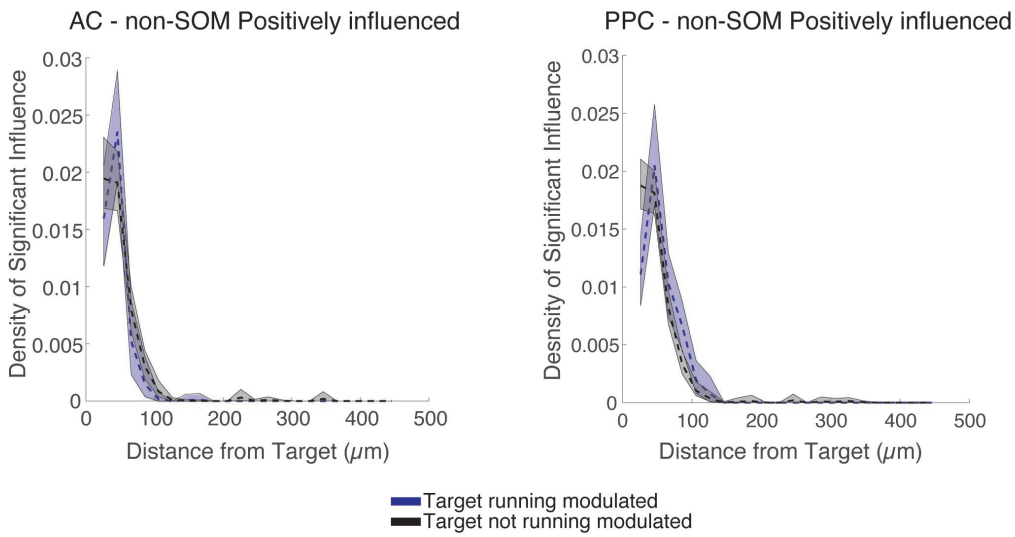

Figure 21 Running Modulated Targets demonstrate a broader spatial range of influence

Spatial distribution of positively influenced non-SOM neurons for targets with running modulation (blue) and targets without running modulation (black). Probability density calculated using non-parametric kernel smoothing function. Shaded regions are 95% bootstrapping confidence intervals. Left: AC. Right: PPC.

4.0 Discussion

4.1 Summary of Findings

We probed the functional network properties of non-SOM and SOM neurons in AC and PPC through a combination of single cell optogenetic stimulation and 2-photon calcium imaging. The resulting effects of the stimulation and running behavior were characterized statistically through a binomial GLM. This approach revealed a strong dependence of the magnitude of influence on distance in both regions yet revealed that magnitude of influence over distance was larger in PPC than in AC for non-SOM cells. Additionally, we demonstrated that the spatial distribution of significantly influenced cells was greater for negatively influenced non-SOM and SOM cells than that of positively influenced non-SOM cells in both AC and PPC. These results suggest a different network of functional connectivity between PYR neurons in PPC and in AC, and that spatial range of inhibitory connections are greater than recurrent excitatory connections in both regions. Additionally, we determined that running modulation in both regions was greatest for non-SOM neurons which were negatively influenced by at least one target which could indicate a relationship between connections to recurrently driven inhibitory neurons and functional response properties.

4.2 Characterization of Influence with a GLM

GLM's have widespread use in systems neuroscience and have contributed to the ability to statistically characterize the relationship between recorded variables and neural activity. We sought to characterize the influence of single cell stimulation through a GLM due to the rigor of the method in addition to the ability to characterize the running modulation of neurons. However, there were a few limitations to the GLM approach in its current manifestation. Primarily, it appeared that the mean session activity of a neuron (calculated outside the stimulation frames) had an impact on the Δfraction explained deviance measurement. The impact of firing rate on our observed results was minimized by adjusting the Δfraction explained deviance measurement by the square root of the firing rate; however, it is possible that there were lingering effects on the data. The relevance of these effects is determined by the question being asked of the data. If the question is simply to characterize the effects of the stimulation on the surrounding cells and to directly compare the magnitude of response between neurons, then the contribution of firing rate to influence could obscure the results because responses of similar magnitudes will be weighted differently. However, if the question being proposed is what the effective change in the network following the stimulation, then firing rate should contribute to the influence measurement because a neuron with a higher firing rate has a less significant deviation from its average activity than a neuron with a lower firing rate and the same magnitude of response. In order to characterize the results from the perspective of the network activity, it would be essential to include the effects of coupling in the model to ensure that the dependence of the target neuron's activity on the influenced cell across all time points is accounted for. Given that coupling is more prevalent and extends over a broader range of distances in PPC than in AC (Khoury, Fala, & Runyan, 2022; Runyan, Piasini, Panzeri, & Harvey, 2017), it would be beneficial to compare how the influence

measurement changes with the addition of coupling as a factor between PPC and AC. The addition of coupling could exaggerate the already observed larger magnitude of influence and broader range of influence observed in PPC as compared to AC, or the broader scale of coupling in PPC could be a manifestation of the differences in functional connectivity observed in this study.

4.3 Relationship of Influence to Distance from Stimulated Target

As has been previously observed in V1 (Chettih & Harvey, 2019; Oldenburg et al., 2024), the magnitude of positive influence decreases rapidly with distance. This dependence of influence on distance was observed in both AC and PPC, yet PPC maintained a larger magnitude of influence over distance than AC. This broader range influence suggests a larger spatial range of functional connections in PPC which is supported by previous work which demonstrated that the spatial range of noise correlations in SOM cells is broader in PPC than in AC (Khoury et al., 2022). This broader range of functional connections has implications for the extent to which PYR neurons in AC and PPC integrate recurrent information. The ability for PYR neurons in PPC to integrate information from a broader range of other PYR neurons reflects its function as a region of sensory integration. The relevance of the broader range of influence in PPC depends on an understanding of the method by which PPC achieves its function as an integrator of sensory modalities. Recent work has demonstrated that the encoding of task and behavior variables is high dimension in PPC and does not tend to aggregate significantly into spatial clusters (Tseng, Chettih, Arlt, Barroso-Luque, & Harvey, 2022). These results promote the hypothesis that behaviorally relevant information is stored through the network state of PPC. If PPC is optimized to convey information through population activity, then the neurons which comprise the network must be able to affect the activity

of surrounding neurons so that they can meaningfully contribute to the network's activity. The role of AC as a sensory cortex theoretically alters the usefulness of a neuron being recurrently connected with a spatially broad range of neurons, yet these results should be considered in relation to the topographic organization in AC. The existence of a tonotopic organization of AC at a broad spatial scale has been well established (Guo et al., 2012), but the sound tuning of neurons in a finer spatial scale has been a subject of debate (Rothschild et al., 2010). Recent work however has demonstrated that the likely source of the disparities in the strength of tonotopic organization at a fine spatial scale is the inclusion criteria for strength of sound tuning (Romero et al., 2020). This difference in tuning organization based on the strength of sound response promotes an interesting question of how the spatial connectivity of neurons in AC differs based on their strength of sound response. Potentially, neurons with a more robust sound response would demonstrate a narrower spatial range of influence with a bias towards similarly tuned neurons while weakly tuned neurons exhibit a broader spatial range of influence. The comparison in this study of the dependence of influence on distance between PPC and AC did not differentiate between neurons with strong sound tuning and those without; therefore, it could be possible that the different dependency on distance between the regions could be exclusive to neurons with strong sound tuning.

Despite the magnitude of influence being highly dependent on distance from the stimulated neuron, the spatial distribution of significantly influenced cells varied substantially from non-SOM cells that were positively influenced to negatively influenced non-SOM and influenced SOM cells. Recent work has supported the finding that the magnitude of influence depends strongly on influence (Oldenburg et al., 2024), yet the relatively broad spatial distribution of negative/SOM influence observed here is still consistent with those findings because the magnitude of negative influence and SOM influence is generally weaker than observed positively influence non-SOM

cells. Additionally, the previously mentioned study examined ensembles of neurons in V1; therefore, the variations in spatial scale of influence and sign of influence could be due to the different properties of PPC and AC as compared to V1. The observed distribution of negative influence supports the hypothesized network connectivity of SOM neurons in PPC (Khoury et al., 2022); however, they hypothesized a larger spatial scale of connectivity for the PYR to SOM network in PPC as compared to AC which was not directly observed in this study. This does not rule out the hypothesis that PYR to SOM connections are broader in PPC than in AC, for it is possible that with more data a relationship would be revealed. Additionally the wider distribution of significant influence for SOM neurons is consistent with the dense interneuron to PYR neuron connectivity within a radius of 200µm found in V1 (Fino & Yuste, 2011). In context of the distribution of SOM influence, the broader spatial scale of negative influence as compared to positive influence is consistent because at least a portion of the negative influence is likely mediated by SOM cells. Therefore, the fact the negative influence is broader than positive could be a reflection of the wider range of PYR to SOM connections over distance.

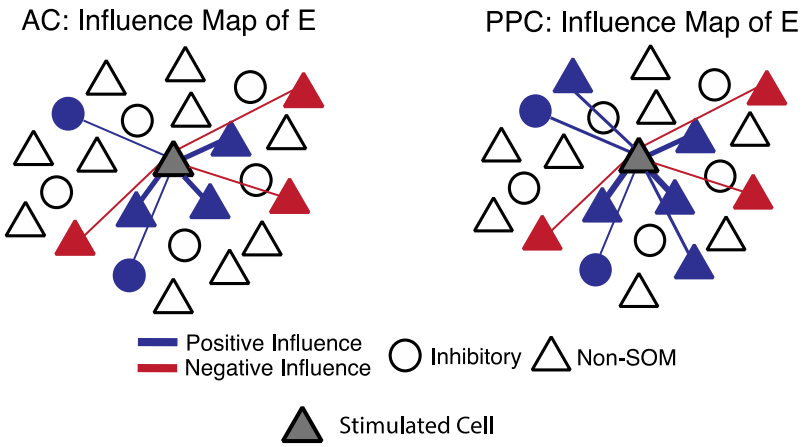

Figure 22: Proposed functional connectivity of E neurons

Strength of proposed connection indicated by line thickness. E refers to excitatory neurons.

4.4 Interaction between Running Modulation and Influence

A motivating factor for characterizing influence with a GLM was the ability to statistically characterize the running modulation of the recorded neurons. Comparing the distribution of running modulations from AC to PPC reaffirmed the previous finding that neurons in PPC are more modulated by running than neurons in AC (Khoury, Fala, & Runyan, 2023). The comparison of running modulation to influence, however, yielded an intriguing cell type and influence sign specific result. Negatively influenced non-SOM cells in AC and PPC both expressed significantly higher running modulation than un-influenced and positively influenced non-SOM/SOM neurons. This result implies a potential connection between the local excitatory to inhibitory network and the network of running influenced cells (Figure 23). These data were collected during passive activity; however, it would be interesting to probe the relationship of local inhibitory effects on running modulated neurons in a task environment as compared to an unstructured environment. Potentially neurons with a higher running modulation are more strongly targeted by local inhibitory networks as a method to damper their running related activity when a higher valance stimuli arrives into the network. Further research is needed to characterize the implications of this bias in running modulation to negatively influenced cells to specifically determine if this bias has a functional role in a task environment.

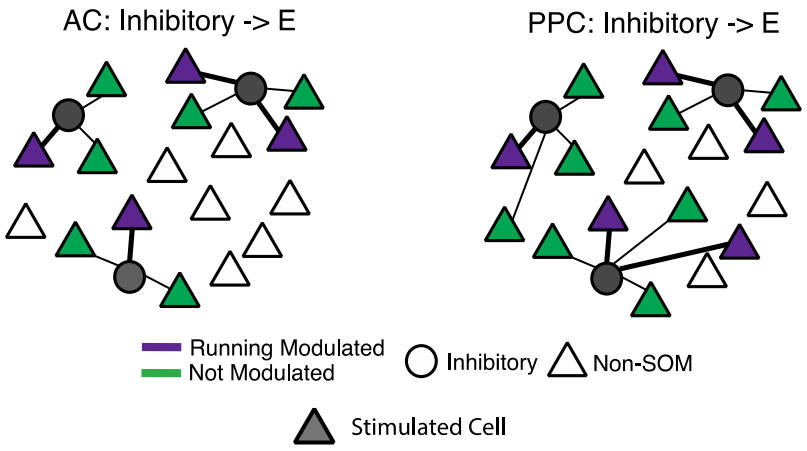

Figure 23 Proposed network of inhibitory neuron to running modulated neurons

Strength of proposed connection indicated by line thickness. E refers to excitatory neurons. Left: AC. Right: PPC. Running modulated cells are proposed to be more strongly inhibited than surrounding E cells not modulated by running.

The relationship of influence to running modulation for a neuron could be affected by the running modulation of the target which influences that cell. A bias for neurons with an overlap of influence and running modulation to have running modulated targets would fit within the conception of similarly driven neurons having a higher probability of connectivity (Ko et al., 2011); however, the percent of neurons which were influenced and modulated by running out of the total number of influenced neurons between modulated and un-modulated targets was only significantly different in AC and not in PPC. This indicates that at least in PPC there is not a network of non-SOM to non-SOM characterized by similarity in running responses. The potential for a network of this architecture does exist in AC which could be due to the lower degree of running modulation in AC overall. A lack of significant bias for shared running modulation between influenced neuron and target in PPC could be explained by the fact that a large amount

of PPC neurons respond in some degree to running, so a selective network cannot form due to the widespread modulation. Contrastingly, in AC, a network of running modulated cells could form between the select AC neurons which do respond to running; however, further characterization of the properties of running modulated neurons in AC is needed to support that hypothesis.

The magnitude of influence did not significantly depend on the relationship of running modulation of the target and influenced neuron (Figure 20), yet there existed a difference in the distribution of significant influence over distance of running modulated targets and un-modulated targets (Figure 21). Targets with running modulation tended to have a broader range of influence than targets without in PPC. This difference was observed in positively influenced non-SOM neurons, so it cannot be attributed to the over representation of negatively influenced cells with running modulation in combination with the slight tendency of running modulated targets to influence running modulated cells. Additionally, this effect was only observed in PPC and not in AC which had a stronger trend of running modulated targets influencing running modulated cells.

4.5 Conclusions

This study demonstrated that the spatial range and magnitude of influence varies between brain regions within the sensory hierarchy, and that across the sensory hierarchy, negative influence and SOM influence has a broader spatial scale than positive influence on non-SOM cells. Additionally, we demonstrated that in both sensory regions, running modulation is highest in non-SOM neurons that were negatively influenced. Future research should be directed to furthering the of understanding the unique functional properties of inhibitory interneuron subclasses within the cortical circuit. Specifically, it would be beneficial to determine if the functional properties of

inhibitory interneuron activity changes in a state dependent way, and if the change in functionality with respect to behavioral or brain state varies across regions in the sensory hierarchy. This study has sought to deepen our understanding of how we perceive the world. A rigorous description of the computations that contribute to perception both enhances our connection to the world and provides a framework that could be used in the future to treat diseases of perception.

Appendix A

Table 1 Means of influence magnitude across distance

Means calculated by post-hoc multiple compare test.

Group	Mean	Error
AC ; non-SOM ; Distance=25-45µm	4.82E-03	6.15E-05
AC ; non-SOM ; Distance=45-65µm	1.51E-03	5.32E-05
AC ; SOM ; Distance=25-45µm	5.42E-03	2.46E-04
AC ; SOM ; Distance=45-65µm	9.07E-04	2.04E-04
PPC ; non-SOM ; Distance=25-45µm	5.16E-03	4.85E-05
PPC ; non-SOM ; Distance=45-65µm	1.92E-03	4.03E-05
PPC ; SOM ; Distance=25-45µm	4.24E-03	1.92E-04
PPC ; SOM ; Distance=45-65µm	1.85E-03	1.52E-04

Table 2 Statistical difference between means of influence over distance

Significance is reported as p value of post-hoc multiple compare test.

Group1	Group2	Significance of Difference in Means
AC ; non-SOM ; Distance=25-45µm	PPC ; non-SOM ; Distance=25-45µm	2.87E-02
AC ; non-SOM ; Distance=45-65µm	PPC ; non-SOM ; Distance=45-65µm	2.50E-06
AC ; SOM ; Distance=25-45µm	PPC ; SOM ; Distance=25-45µm	2.41E-01
AC ; SOM ; Distance=45-65µm	PPC ; SOM ; Distance=45-65µm	2.84E-01
AC ; non-SOM ; Distance=25-45µm	AC ; SOM ; Distance=25-45µm	9.99E-01
AC ; non-SOM ; Distance=45-65µm	AC ; SOM ; Distance=45-65µm	9.52E-01
PPC ; non-SOM ; Distance=25-45µm	PPC ; SOM ; Distance=25-45µm	8.97E-03
PPC ; non-SOM ; Distance=45-65µm	PPC ; SOM ; Distance=45-65µm	1.00E+00

Appendix B

Table 3 Means of running modulation: AC

Means and error calculated by post-hoc multiple compare test.

Group	Mean	Error
Not-influenced non-SOM	0.0049	6.17E-05
Positively Influenced non-SOM	0.0097	4.12E-04
Negatively Influenced non-SOM	0.0264	8.22E-04
Not-Influence SOM	0.006	2.55E-04
Positively Influence SOM	0.0079	0.0017
Negatively Influenced SOM	0.0092	0.0023

Table 4 Statistical difference between means of running modulation: AC

Significance is reported as p value of post-hoc multiple compare test.

Group1	Group2	Significance of Difference in Means
Not-influenced , non-SOM	Negatively influenced, non-SOM	0
Positively influenced, non-SOM	Negatively influenced, non-SOM	0
Negatively influenced, SOM	Negatively influenced, non-SOM	1.98E-11

Table 5 Means of running modulation: PPC

Means and error calculated by post-hoc multiple compare test.

Group	Mean	Error
Not-influenced non-SOM	0.0154	2.36E-04
Positively Influenced non-SOM	0.0129	7.26E-04
Negatively Influenced non-SOM	0.0329	0.0012
Not-Influence SOM	0.0166	8.80E-04
Positively Influence SOM	0.0146	0.0029
Negatively Influenced SOM	0.0123	0.0068

Table 6 Statistical difference between means of running modulation: PPC

Significance is reported as p value of post-hoc multiple compare test.

Group1	Group2	Significance of Difference in Means
not influenced , non-SOM	negatively influenced, non-SOM	0
positively influenced, non-SOM	negatively influenced, non-SOM	0
negatively influenced, SOM	negatively influenced, non-SOM	0.03787157266

Bibliography

Adesnik, H., Bruns, W., Taniguchi, H., Huang, Z. J., & Scanziani, M. (2012). A neural circuit for spatial summation in visual cortex. *Nature, 490*(7419), 226-231. doi:10.1038/nature11526

Banich, M. T., & Compton, R. J. (2023). *Cognitive Neuroscience* (5 ed.). Cambridge: Cambridge University Press.

Chettih, S. N., & Harvey, C. D. (2019). Single-neuron perturbations reveal feature-specific competition in V1. *Nature, 567*(7748), 334-340. doi:10.1038/s41586-019-0997-6

Colby, C. L., & Goldberg, M. E. (1999). SPACE AND ATTENTION IN PARIETAL CORTEX. *Annual review of neuroscience, 22*(1), 319-349. doi:10.1146/annurev.neuro.22.1.319

Douglas, R. J., & Martin, K. A. C. (2004). NEURONAL CIRCUITS OF THE NEOCORTEX. *Neuroscience, 27*(1), 419-451. doi:10.1146/annurev.neuro.27.070203.144152

Fanselow, E. E., Richardson, K. A., & Connors, B. W. (2008). Selective, State-Dependent Activation of Somatostatin-Expressing Inhibitory Interneurons in Mouse Neocortex. *Journal of Neurophysiology, 100*(5), 2640-2652. doi:10.1152/jn.90691.2008

Fino, E., & Yuste, R. (2011). Dense Inhibitory Connectivity in Neocortex. *Neuron, 69*(6), 1188-1203. doi:10.1016/j.neuron.2011.02.025

Francis, N. A., Winkowski, D. E., Sheikhattar, A., Armengol, K., Babadi, B., & Kanold, P. O. (2018). Small Networks Encode Decision-Making in Primary Auditory Cortex. *Neuron, 97*(4), 885-897.e886. doi:10.1016/j.neuron.2018.01.019

Friedman, J., Hastie, T., & Tibshirani, R. (2010). Regularization Paths for Generalized Linear Models via Coordinate Descent. *Journal of Statistical Software, 33*(1). doi:10.18637/jss.v033.i01

Friedrich, J., Zhou, P., & Paninski, L. (2017). Fast online deconvolution of calcium imaging data. *PLoS Computational Biology, 13*(3), e1005423. doi:10.1371/journal.pcbi.1005423

Green, J., Bruno, C. A., Traunmüller, L., Ding, J., Hrvatin, S., Wilson, D. E., . . . Harvey, C. D. (2023). A cell-type-specific error-correction signal in the posterior parietal cortex. *Nature, 620*(7973), 366-373. doi:10.1038/s41586-023-06357-1

Guo, W., Chambers, A. R., Darrow, K. N., Hancock, K. E., Shinn-Cunningham, B. G., & Polley, D. B. (2012). Robustness of Cortical Topography across Fields, Laminae, Anesthetic States, and Neurophysiological Signal Types. *Journal of Neuroscience, 32*(27), 9159-9172. doi:10.1523/jneurosci.0065-12.2012

Harris, K. D., & Mrsic-Flogel, T. D. (2013). Cortical connectivity and sensory coding. *Nature, 503*(7474), 51-58. doi:10.1038/nature12654

Harvey, C. D., Coen, P., & Tank, D. W. (2012). Choice-specific sequences in parietal cortex during a virtual-navigation decision task. *Nature, 484*(7392), 62-68. doi:10.1038/nature10918

Herzog, M. H., & Clarke, A. M. (2014). Why vision is not both hierarchical and feedforward. *Frontiers in Computational Neuroscience, 8*, 135. doi:10.3389/fncom.2014.00135

Hovde, K., Gianatti, M., Witter, M. P., & Whitlock, J. R. (2018). Architecture and organization of mouse posterior parietal cortex relative to extrastriate areas. *bioRxiv*, 361832. doi:10.1101/361832

Khoury, C. F., Fala, N. G., & Runyan, C. A. (2022). The spatial scale of somatostatin subnetworks increases from sensory to association cortex. *Cell Reports, 40*(10), 111319. doi:10.1016/j.celrep.2022.111319

Khoury, C. F., Fala, N. G., & Runyan, C. A. (2023). Arousal and Locomotion Differently Modulate Activity of Somatostatin Neurons across Cortex. *eNeuro, 10*(5), ENEURO.0136-0123.2023. doi:10.1523/eneuro.0136-23.2023

Ko, H., Hofer, S. B., Pichler, B., Buchanan, K. A., Sjöström, P. J., & Mrsic-Flogel, T. D. (2011). Functional specificity of local synaptic connections in neocortical networks. *Nature, 473*(7345), 87-91. doi:10.1038/nature09880

Lee, W.-C. A., Bonin, V., Reed, M., Graham, B. J., Hood, G., Glattfelder, K., & Reid, R. C. (2016). Anatomy and function of an excitatory network in the visual cortex. *Nature, 532*(7599), 370-374. doi:10.1038/nature17192

Ma, Y., Hu, H., & Agmon, A. (2012). Short-Term Plasticity of Unitary Inhibitory-to-Inhibitory Synapses Depends on the Presynaptic Interneuron Subtype. *The Journal of Neuroscience, 32*(3), 983-988. doi:10.1523/jneurosci.5007-11.2012

Natan, R. G., Briguglio, J. J., Mwilambwe-Tshilobo, L., Jones, S. I., Aizenberg, M., Goldberg, E. M., & Geffen, M. N. (2015). Complementary control of sensory adaptation by two types of cortical interneurons. *eLife, 4*, e09868. doi:10.7554/elife.09868

O'Keefe, J., & Dostrovsky, J. (1971). The hippocampus as a spatial map. Preliminary evidence from unit activity in the freely-moving rat. *Brain Research, 34*(1), 171-175. doi:10.1016/0006-8993(71)90358-1

Oláh, S., Füle, M., Komlósi, G., Varga, C., Báldi, R., Barzó, P., & Tamás, G. (2009). Regulation of cortical microcircuits by unitary GABA-mediated volume transmission. *Nature, 461*(7268), 1278-1281. doi:10.1038/nature08503

Oldenburg, I. A., Hendricks, W. D., Handy, G., Shamardani, K., Bounds, H. A., Doiron, B., & Adesnik, H. (2024). The logic of recurrent circuits in the primary visual cortex. *Nature Neuroscience, 27*(1), 137-147. doi:10.1038/s41593-023-01510-5

Pachitariu, M., Stringer, C., Dipoppa, M., Schröder, S., Rossi, L. F., Dalgleish, H., . . . Harris, K. D. (2017). Suite2p: beyond 10,000 neurons with standard two-photon microscopy. *bioRxiv*, 061507. doi:10.1101/061507

Pfeffer, C. K., Xue, M., He, M., Huang, Z. J., & Scanziani, M. (2013). Inhibition of inhibition in visual cortex: the logic of connections between molecularly distinct interneurons. *Nature Neuroscience, 16*(8), 1068-1076. doi:10.1038/nn.3446

Romero, S., Hight, A. E., Clayton, K. K., Resnik, J., Williamson, R. S., Hancock, K. E., & Polley, D. B. (2020). Cellular and Widefield Imaging of Sound Frequency Organization in Primary and Higher Order Fields of the Mouse Auditory Cortex. *Cerebral Cortex, 30*(3), 1603-1622. doi:10.1093/cercor/bhz190

Rothschild, G., Nelken, I., & Mizrahi, A. (2010). Functional organization and population dynamics in the mouse primary auditory cortex. *Nature Neuroscience, 13*(3), 353-360. doi:10.1038/nn.2484

Runyan, C. A., Piasini, E., Panzeri, S., & Harvey, C. D. (2017). Distinct timescales of population coding across cortex. *Nature, 548*(7665), 92-96. doi:10.1038/nature23020

Stiebler, I., Neulist, R., Fichtel, I., & Ehret, G. (1997). The auditory cortex of the house mouse: left-right differences, tonotopic organization and quantitative analysis of frequency representation. *Journal of Comparative Physiology A, 181*(6), 559-571. doi:10.1007/s003590050140

Tseng, S.-Y., Chettih, S. N., Arlt, C., Barroso-Luque, R., & Harvey, C. D. (2022). Shared and specialized coding across posterior cortical areas for dynamic navigation decisions. *Neuron, 110*(15), 2484-2502.e2416. doi:10.1016/j.neuron.2022.05.012

Walsh, K. S., McGovern, D. P., Clark, A., & O'Connell, R. G. (2020). Evaluating the neurophysiological evidence for predictive processing as a model of perception. *Annals of the New York Academy of Sciences, 1464*(1), 242-268. doi:10.1111/nyas.14321

Wehr, M., & Zador, A. M. (2003). Balanced inhibition underlies tuning and sharpens spike timing in auditory cortex. *Nature, 426*(6965), 442-446. doi:10.1038/nature02116

Xu, H., Jeong, H.-Y., Tremblay, R., & Rudy, B. (2013). Neocortical Somatostatin-Expressing GABAergic Interneurons Disinhibit the Thalamorecipient Layer 4. *Neuron, 77*(1), 155-167. doi:10.1016/j.neuron.2012.11.004

Yavorska, I., & Wehr, M. (2016). Somatostatin-Expressing Inhibitory Interneurons in Cortical Circuits. *Frontiers in Neural Circuits, 10*, 76. doi:10.3389/fncir.2016.00076

Yoshimura, Y., Dantzker, J. L. M., & Callaway, E. M. (2005). Excitatory cortical neurons form fine-scale functional networks. *Nature, 433*(7028), 868-873. doi:10.1038/nature03252

Yoshitake, K., Tsukano, H., Tohmi, M., Komagata, S., Hishida, R., Yagi, T., & Shibuki, K. (2013). Visual Map Shifts based on Whisker-Guided Cues in the Young Mouse Visual Cortex. *Cell Reports, 5*(5), 1365-1374. doi:10.1016/j.celrep.2013.11.006

Zhang, S., Xu, M., Chang, W.-C., Ma, C., Do, J. P. H., Jeong, D., . . . Dan, Y. (2016). Organization of long-range inputs and outputs of frontal cortex for top-down control. *Nature Neuroscience, 19*(12), 1733-1742. doi:10.1038/nn.4417